Article+

Developmental Cell

Sequential Contraction and Exchange of Apical Junctions Drives Zippering and Neural Tube Closure in a Simple Chordate

Highlights

- Unidirectional zippering is required for neural tube closure
- Sequential activation of junctional myosin drives posterior-to-anterior zippering
- Local coupling of junction shortening and rearrangement makes zippering directional
- Computer simulations support the sufficiency of a sequential contraction mechanism

Authors

Hidehiko Hashimoto, Francois B. Robin, Kristin M. Sherrard, Edwin M. Munro

Correspondence

robin@crans.org (F.B.R.), emunro@uchicago.edu (E.M.M.)

In Brief

Neural tube closure is a critical morphogenetic process in chordate embryonic development. Combining experimental analysis and computer simulation, Hashimoto, Robin, et al. show how local myosin activation and junctional rearrangements together produce directional zippering to drive neural tube closure in a basal chordate. Similar mechanisms may operate in vertebrate neurulation.

Hashimoto et al., 2015, Developmental Cell *32*, 241–255
January 26, 2015
http://dx.doi.org/10.1016/j.devcel.2014.12.017

CellPress

Developmental Cell
Article+

Sequential Contraction and Exchange of Apical Junctions Drives Zippering and Neural Tube Closure in a Simple Chordate

Hidehiko Hashimoto,[1,5] Francois B. Robin,[1,2,4,5,*] Kristin M. Sherrard,[1] and Edwin M. Munro[1,2,3,*]
[1]Department of Molecular Genetics and Cell Biology, University of Chicago, Chicago, IL 60637, USA
[2]Committee on Development, Regeneration and Stem Cell Biology, University of Chicago, Chicago, IL 60637, USA
[3]Institute for Biophysical Dynamics, University of Chicago, Chicago, IL 60637, USA
[4]Present address: Institute for Biology Paris-Seine, University Pierre et Marie Curie, 75252 Paris, France
[5]Co-first author
*Correspondence: robin@crans.org (F.B.R.), emunro@uchicago.edu (E.M.M.)
http://dx.doi.org/10.1016/j.devcel.2014.12.017

SUMMARY

Unidirectional zippering is a key step in neural tube closure that remains poorly understood. Here, we combine experimental and computational approaches to identify the mechanism for zippering in a basal chordate, *Ciona intestinalis*. We show that myosin II is activated sequentially from posterior to anterior along the neural/epidermal (Ne/Epi) boundary just ahead of the advancing zipper. This promotes rapid shortening of Ne/Epi junctions, driving the zipper forward and drawing the neural folds together. Cell contact rearrangements (Ne/Epi + Ne/Epi → Ne/Ne + Epi/Epi) just behind the zipper lower tissue resistance to zipper progression by allowing transiently stretched cells to detach and relax toward isodiametric shapes. Computer simulations show that measured differences in junction tension, timing of primary contractions, and delay before cell detachment are sufficient to explain the speed and direction of zipper progression and highlight key advantages of a sequential contraction mechanism for robust efficient zippering.

INTRODUCTION

Neurulation is one of the defining events of chordate morphogenesis, in which the neural tube forms and separates from a surface epidermis to form the rudiment of the future nervous system. Failures in neurulation are a leading cause of birth defects in humans, affecting more than 1 in 1,000 pregnancies in human populations (reviewed in Copp et al., 2013; Wallingford et al., 2013). Molecular and genetic approaches have identified a growing list of genes whose disruption leads to defects in neural tube closure (Copp and Greene, 2010). However, it remains a fundamental challenge to understand the origin of forces that drive neurulation, how these forces are patterned in space and time, and how they are integrated to orchestrate robust formation and closure of the neural tube.

Studies across chordates have identified three largely conserved steps that transform an initially flat neuroectodermal sheet called the neural plate into a closed and elongated neural tube (reviewed in Schoenwolf and Smith, 1990; Wallingford et al., 2013; Yamaguchi and Miura, 2013). The neural plate first bends about medial and lateral hinge points to form a furrow with elevated neural folds bordering the lateral neuroectoderm. The neural primordium then converges medially and extends axially, bringing the neural folds closer to the presumptive midline. Finally, the neural folds meet, fuse, and remodel at the midline to separate a closed neural tube from a continuous overlying epidermis. This last step initiates at one or more specific positions and then proceeds in a directional manner and has thus been referred to as neural tube zippering (herein, "zippering") (Nicol and Meinertzhagen, 1988a, 1988b; Jaskoll et al., 1991; Pyrgaki et al., 2010; Yamaguchi et al., 2011; Massarwa and Niswander, 2013; reviewed in Colas and Schoenwolf, 2001).

The first two steps in neurulation have been extensively studied, and their molecular, cellular, and mechanical bases are increasingly well understood. The initial invagination is driven largely by actomyosin-dependent apical constriction, which is controlled in space and time by a number of key regulators including members of the Shroom family and the planar cell polarity pathway (Hildebrand and Soriano, 1999; Wallingford and Harland, 2002; Haigo et al., 2003; Hildebrand, 2005; Nishimura and Takeichi, 2008; Nishimura et al., 2012). Convergence and extension of the neural primordium are driven by a mixture of cellular behaviors, including oriented cell divisions (Sausedo et al., 1997), mediolateral intercalation driven by polarized cell crawling (reviewed in Wallingford et al., 2002), and active shortening of apical cell-cell junctions (Nishimura et al., 2012). The relative contributions of these behaviors vary regionally within the same embryo and across chordates. In addition to forces generated within the neural tube, extrinsic forces generated within the nonneural ectoderm may also contribute to pushing the neural folds together (Alvarez and Schoenwolf, 1992; Morita et al., 2012).

In contrast, neural tube zippering has received less attention. Most work to date has focused on how fusion and separation of neural and epidermal tissues might occur through dynamic modulation of junctional signaling, cell-cell adhesion, and local cell death (Yamaguchi et al., 2011; reviewed in Ray and

Niswander, 2012; Yamaguchi and Miura, 2013). Previous studies have implicated a variety of molecular players in these processes, including cadherins (Hatta and Takeichi, 1986; Bronner-Fraser et al., 1992), ephrin/Eph signaling (Holmberg et al., 2000), and protease-activated receptor kinase signaling (Camerer et al., 2010; reviewed in Pai et al., 2012; Ray and Niswander, 2012). However, the underlying cell biology is poorly understood, and it remains largely unclear what forces drive zippering, what makes it directional and governs its speed, and to what extent zippering contributes mechanically to neural tube closure. Recent live imaging studies in mouse embryos have begun to address these questions by documenting cell shape changes and local motile behaviors that correlate with zippering (Pyrgaki et al., 2010; Yamaguchi et al., 2011; Massarwa and Niswander, 2013), but these have yet to be fit into a mechanistic view of zipper progression.

Ascidians provide an opportunity to investigate zippering and neural tube closure in a simple and experimentally tractable embryonic context. Like many vertebrates, ascidians form a neural tube through the invagination of an initially flat epithelium, followed by convergent extension and then fusion of the neural folds (zippering) in a posterior-to-anterior progression (Nicol and Meinertzhagen, 1988a, 1988b). However, unlike higher vertebrates, they do so in less than 2 hr, with ~40 neural cells, in embryos with invariant lineages (Nishida 1987; Nicol and Meinertzhagen, 1988a, 1988b) and highly stereotyped early development, whose small size and optical clarity make them amenable to physical manipulation and computer simulation (Sherrard et al., 2010).

Here, we combine quantitative microscopy with physical, molecular genetic, and pharmacological manipulations and computer simulations to identify the cytomechanical basis for zippering and neural tube closure in the ascidian *Ciona intestinalis*. We show that zippering provides an essential driving force for neural tube closure and that it is powered by a repeated cycle of apical junction contraction and exchange that sweeps from posterior to anterior along the neural/epidermal (Ne/Epi) boundary. Rho kinase (ROCK)-dependent myosin activation drives rapid junctional shortening just ahead of the zipper; dynamic rearrangement of apical junctions (Ne/Epi + Ne/Epi → Ne/Ne + Epi/Epi) at/behind the zipper allows cells stretched by the advancing zipper to detach and relax. This creates a dynamic imbalance of anterior versus posterior tissue resistance that converts a local increase in contractile tension just ahead of the zipper into asymmetrical junctional shortening and unidirectional zipper progression. Computer simulations confirm the sufficiency of this mechanism to explain the observed kinematics of zipper progression, reveal key determinants of zippering speed, and highlight the advantages of sequential contraction for efficient closure. We suggest that similar mechanisms may govern zippering and neural tube closure in higher vertebrates, including humans.

RESULTS

We begin with a brief overview and timeline of ascidian neurulation (Figure 1; Movie S1 available online). Just before neurulation, the neural plate is a flat monolayer sheet containing ~40 cells (Nicol and Meinertzhagen, 1988a). The posterior neural plate (blue in Figure 1B) gives rise to the axial nerve cord, while the anterior neural plate (green in Figure 1B) gives rise to the sensory vesicle. The posterior neural plate first invaginates in a posterior-to-anterior wave (Nicol and Meinertzhagen, 1988b; Movie S1), then closes though posterior-to-anterior zippering to form an elongated tube (Figure 1D). In contrast, the anterior neural plate invaginates with radial symmetry to form a shallow cup (Figure 1C), which then closes symmetrically to form a spherical cyst.

Zippering Provides an Essential Driving Force for Neural Tube Closure

In this study, we focused on zippering and closure of the posterior neural tube. In initial time-lapse observations, we observed a tight correlation between zipper progression and movement of neural folds toward the midline (Figure 1B; Movie S1), suggesting that zippering might provide an essential driving force for neural tube closure. To test this, we cut embryos into anterior and posterior halves just before the initiation of zippering (Figures 2A, 2C, and 2E) and then analyzed the behaviors of the cut halves relative to similarly staged controls. Confocal analysis of anterior half-embryos fixed at stage 18 (Hotta et al., 2007), when zippering was complete in control embryos, showed a complete failure to close the neural tube in 17/20 cases (Figures 2B and 2D). Time-lapse analysis of the anterior half-embryos showed that invagination progressed normally anterior to the cut, but the neural folds failed to approach the midline, and the neural tube remained open well after the neural tube had closed in wild-type embryos (Figures 2B′ and 2D′; Movie S2). In contrast, 20/22 of posterior half-embryos completed neural tube closure up to the anterior cut point (Figures 2E and 2F); cross-sectional views revealed a normally structured neural tube (compare Figures 2B″ and 2F′), and time-lapse analysis showed that this occurred by zippering at a normal speed relative to controls (Movie S2). We conclude that invagination of the neural plate and zipper progression are separable processes, but zipper progression is absolutely required for neural tube closure.

A Characteristic Sequence of Local Cell Behaviors Accompanies Zipper Progression

To identify cell behaviors that underlie zippering, we performed quantitative time-lapse analysis of embryos expressing the tight junction marker ZO1-3xGFP under control of the neural and epidermal-specific promoter pFOG, which expresses in all epidermal cells and in lateral neural plate cells just adjacent to the epidermis (Pasini et al., 2006). ZO1-3xGFP labels punctate structures along all cell-cell junctions just below the apical surface, allowing us to assess junctional deformations in relation to zipper progression with subcellular resolution (Movie S3).

Strikingly, we found that zipper progression was correlated with the rapid and sequential shortening of individual junctions along the Ne/Epi boundary proceeding from posterior to anterior just ahead of the advancing zipper (solid color lines in Figure 3A; Movie S3). This pattern was readily apparent in individual embryos. Junctions just ahead of the zipper (herein, "primary junctions") shortened in an all-or-none fashion at an average speed of 0.032 ± 0.012 μm/s and usually (but not always) proceeded to completion before the next junction (herein, "secondary junctions") began to shorten, with an average delay of 504 ± 324 s between the initiation of consecutive contractions (Figures 3B and S3C). Rapid contractions of primary junctions were

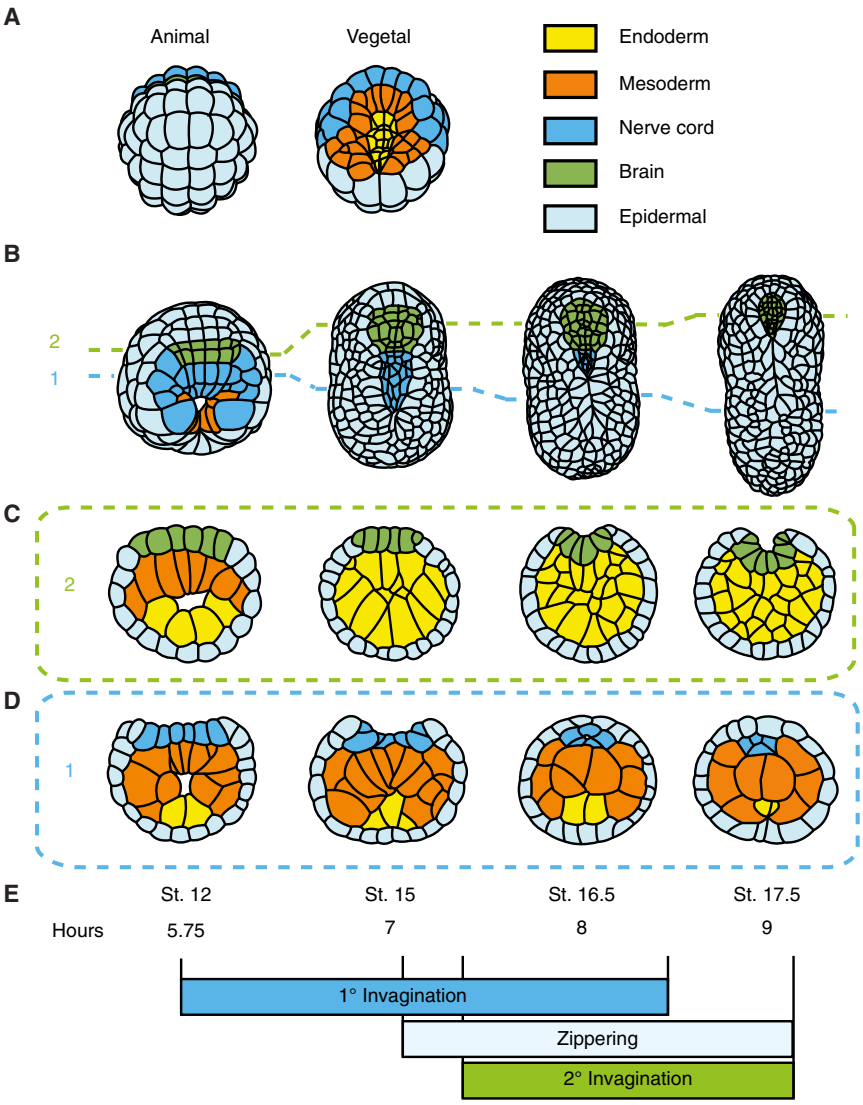

Figure 1. Neural Tube Closure Proceeds by a Combination of Ectoderm Invagination and Zippering

(A) Animal and vegetal views of the 118-cell (early gastrula) stage showing presumptive tissue domains: yellow = endoderm; orange = mesoderm; blue = nerve cord; green = brain; light blue = epidermis. Anterior is up.

(B–D) Embryos at the 12, 15, 16.5, and 17.5 stages, respectively. (B) Dorsal view; anterior is up. (C and D) Transverse sections taken at dotted lines 2 (green, C) and 1 (blue, D) as indicated in (B), through the brain and nerve cord, respectively. Dorsal is up.

(E) Summarizes the time course of neurulation and the corresponding initiation of first invagination of the nerve cord (as seen in D), zippering, and second invagination of the brain (as seen in C).

sometimes accompanied by stretching of their anterior neighbors (left arrow in Figure 3B); occasionally, primary and secondary junctions contracted together (right arrow in Figure 3B). Measurements of average junctional shortening speed as a function of junction position *relative* to the zipper are consistent with these observations (Figure 3C): On average, only primary junctions underwent significant shortening, while secondary junctions shortened slightly, reflecting the balance of mild stretching and occasional shortening observed on individual junctions. During primary junctional shortening events, the zipper moved forward by an average of 126% ± 38% of the original junction length, projected onto the antero-posterior (AP) axis (Figure 3D), but remained close to the midline, such that the anterior end of each junction moved to the midline as the junction shortened.

We also observed a characteristic sequence of cell shape changes behind the zipper (Figure 3A; Movie S3). As newly met Ne/Epi cells exchange junctions, they remain connected to the zipper by cellular tethers and their apices become progressively stretched along the AP axis as the zipper advances past them. Completion of junctional exchange could be detected as a rapid retraction of the tether and relaxation of the cell apex toward a more isodiametric shape (Figure 3E), accompanied by appearance and elongation of a new Epi/Epi junction just behind the advancing zipper (dashed lines in Figure 3A). In general, cells detached from the zipper in the same order that they joined, i.e., in a posterior-to-anterior progression, although we sometimes observed near-simultaneous detachment events (Figure 3E; Movie S3).

In summary, we find that a characteristic sequence of cell shape changes and rearrangements proceeds posterior to anterior in phase with zipper progression and neural tube closure. Just ahead of the zipper, rapid shortening of Ne/Epi junctions correlates tightly with zipper advance and with movement of neural folds to the midline. Just behind the zipper, neural and epidermal cells undergo transient stretching followed by junctional rearrangement, detachment and rapid cell shape relaxation.

Actomyosin Is Enriched Just ahead of the Advancing Zipper where Rapid Junctional Contraction Occurs

We hypothesized that local activation/accumulation of actomyosin might be involved in junctional shortening during zippering, as in many other developmental contexts (reviewed in Guillot and Lecuit, 2013). In nonmuscle cells, actomyosin contractility is activated by phosphorylation of the nonmuscle myosin II regulatory light chain at Ser19 (Komatsu and Ikebe, 2004; reviewed in Matsumura, 2005). We therefore examined the distribution of Ser19-phosphorylated myosin II (herein, "active myosin") in fixed immunostained embryos (Figure 4A; Sherrard et al., 2010). We detected active myosin at all cell-cell junctions in neurula-stage embryos. During zippering, active myosin was slightly enriched along the entire Ne/Epi boundary relative to more lateral junctions between epidermal cells and highly enriched just ahead of the advancing zipper (arrowhead in Figure 4A, left).

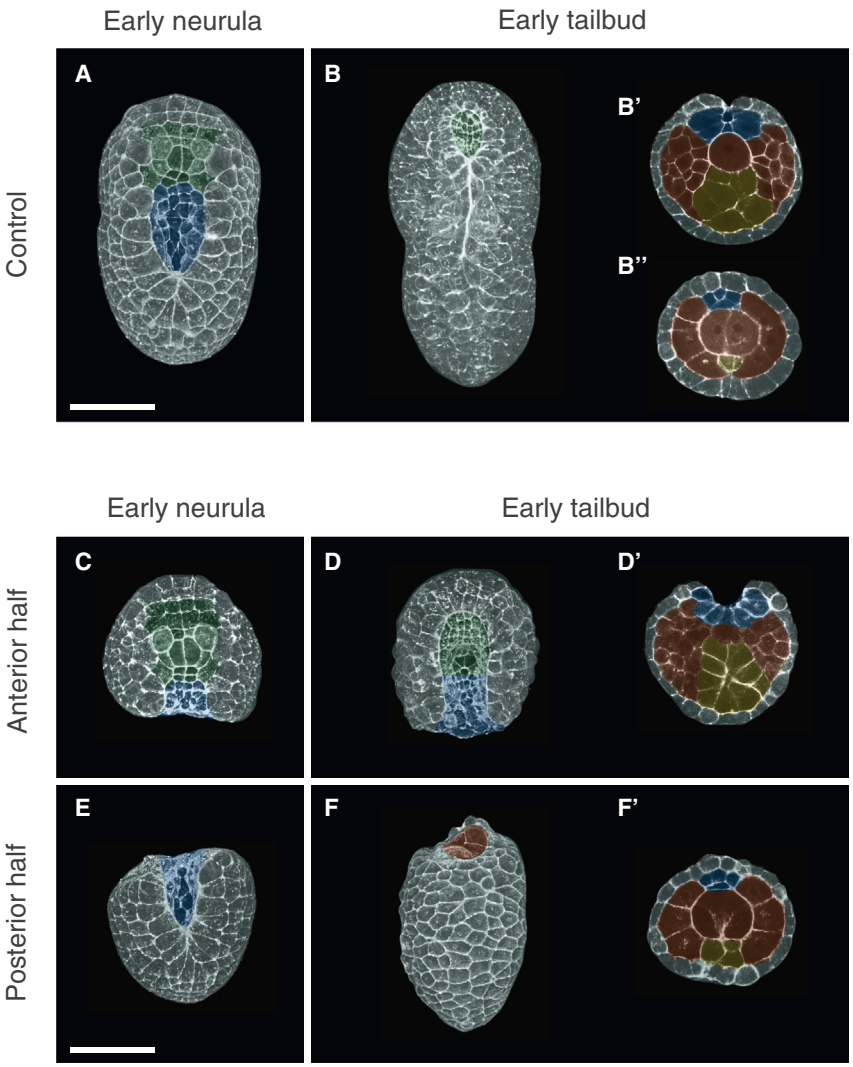

Figure 2. Zippering Is Required to Close the Neural Tube

Control and ablated embryos were fixed, stained with phalloidin, and imaged at early neurula stage when ablation was performed (left column) or at early tailbud stage (middle and right column). Left and middle columns: 3D rendering of the dorsal side, with anterior at the top. Right column: cross-section along the antero-posterior (AP) axis, with dorsal at the top. Yellow, endoderm; orange, mesoderm; blue, nerve cord; green, brain; light blue, epidermis. Scale bars, 50 μm.

(A–B″) Control embryos.

(C–D′) Anterior half-embryo explants.

(E–F′) Posterior half-embryo explants.

(B′ and D′) Cross-section through anterior nerve cord.

(B″ and F′) Cross-section through posterior nerve cord.

Active myosin was also enriched on newly formed Epi/Epi junctions behind the zipper (arrowhead in Figure 4A, middle). Quantitation of fluorescence intensities in embryos fixed during zippering confirmed that, on average, myosin was specifically and highly enriched on junctions just ahead of the advancing zipper (Figure 4B). Filamentous actin (F-actin) was also enriched along the entire Ne/Epi boundary and newly formed Epi/Epi junctions (Figures S1A and S1B). However, in contrast to active myosin, we could detect no specific enrichment of F-actin just ahead of the advancing zipper.

Next, we sought to observe myosin II dynamics in live embryos during zippering. Our attempts to express GFP-tagged myosin II regulatory light chain in early-neurula-stage embryos were unsuccessful. As an alternative approach (Chaigne et al., 2013), we used a yellow fluorescent protein (YFP)-tagged intrabody (herein, "iMyo-YFP") that recognizes nonmuscle myosin II A (Nizak et al., 2003) through an epitope that is highly conserved in *Ciona intestinalis* (Vielemeyer et al., 2010; Figure S1C). The iMyo-YFP accumulated dynamically at the cleavage furrow during cell division (Figure S1D), and subcellular distributions of iMyo-YFP in fixed embryos closely matched those for active (1P) myosin II detected by immunostaining (Figure S1E). On average, iMyo-YFP was highly enriched on Ne/Epi junctions just ahead of the zipper, as observed for 1P myosin (Figure S1F). In live embryos expressing iMyo-YFP during zippering, fluorescence intensity increased sharply within rapidly contracting junctions just ahead of the zipper (Figures 4C and S1G; Movie S4). We also observed occasional transient accumulations of iMyo-YFP that coincided with transient junction contractions at more anterior positions along the Ne/Epi boundary (data not shown). We focused on the subset of primary junction contraction events (n = 12 events from 5 embryos) for which the onset of shortening could be readily detected following a period of approximately constant length (see Experimental Procedures). Aligning fluorescence intensity data with respect to the onset of rapid contraction for these events showed that, on average, the onset of iMyo-YFP accumulation coincided with the onset of rapid contraction (Figure 4D). A similar correlation could be observed for many individual junctions, although the data were noisier, presumably reflecting fluctuations in external force due to contraction of neighboring junctions or detachment of cells from the zipper (Figures 4C and S1G). In summary, we find that active myosin is highly and specifically enriched along junctions that undergo rapid shortening, and the enrichment is closely phased with the onset of contraction, suggesting a direct role for actomyosin contractility in driving junctional shortening, zippering, and neural tube closure.

Rho/ROCK-Dependent Actomyosin Contractility Is Required for Zippering and Neural Tube Closure

To test this possibility, we treated embryos with 100 μM blebbistatin, a small molecule inhibitor of myosin II ATPase activity

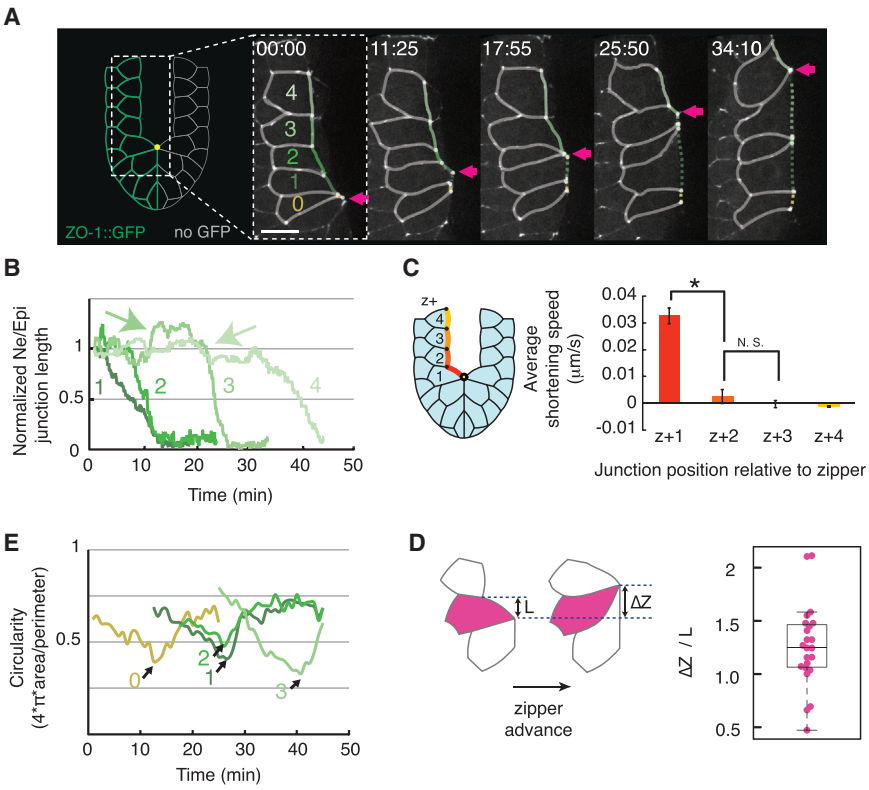

Figure 3. Quantitative Analysis of Cell Shape Changes during Zipper Progression

(A) Schematic on the left shows the location in the embryo of the epidermal cells imaged on the right. On the right, images extracted from Movie S3, show an embryo expressing ZO1-3xGFP in epidermal and neural cells. Note that expression of ZO1-3xGFP is mosaic and restricted to the left half of the embryo. Filled magenta circles indicate zipper position. Epidermal cells sharing an apical junction with the nerve cord have been outlined in white for Epi/Epi junctions, outlined in color for Ne/Epi or newly formed Epi/Epi junctions, and numbered (0–4). Light brown: cell that has already finished contracting. Dark to light green corresponds to absolute AP position. Solid and dashed lines indicate Ne/Epi junctions and junction exchanged Epi/Epi junctions, respectively.

(B) Normalized length versus time for the Ne/Epi junctions highlighted in (A), using the same color code. Rightward-pointing green arrow indicates a secondary junction (3) that stretches when the primary junction (2) contracts; leftward-pointing green arrow indicates a secondary junction (4) that contracts transiently in unison with the primary junction (3).

(C) Left: embryo schematic indicating positions of distinct junction types. Red-yellow is proximal-distal Ne/Epi junction position relative to the zipper. Right: shortening speed of Ne/Epi junctions, with respect to the relative position to the zipper. The shortening speed is measured during the period in which the Ne/Epi junction next to the zipper (z + 1) starts and finishes its contraction. *p < 0.002, Student's t test. Error bars are SEM (n = 23, from seven embryos).

(D) Left: design of the measurement for zipper-advance ratio. L is the length of the junction, as projected along the AP axis, and ΔZ is corresponding distance traversed by the advancing zipper. Right: box and whisker plots showing the distribution of ratio of junction length change to zipper advance. Red circles indicate individual measurements for a single cell (n = 23 cells, from seven embryos).

(E) Circularity of junction-exchanged epidermal cells from Movie S2. Colors are the same as in (A). Black arrows indicate junction detachment points. Scale bars, 5 μm.

(Straight et al., 2003), just after the posterior neural plate had invaginated, but before the onset of zippering. In blebbistatin-treated embryos, we observed a complete inhibition of zippering and anterior neural plate invagination, together with an expansion of the apical surfaces of previously invaginated posterior neural cells, resulting in an open neural tube (Figure 4E; Movie S5). These results suggest that myosin activity is required for both invagination and zippering but do not exclude the possibility that the failure of zippering is indirectly caused by apical expansion of the neural plate. To test this, we treated embryos at the same stage with 1 μM H1152, a highly potent and specific inhibitor of ROCK (Ikenoya et al., 2002), which activates myosin II by promoting phosphorylation of the myosin regulatory light chain (Winter et al., 2001; Marlow et al., 2002). In H1152-treated embryos, we observed a complete inhibition of both zipper progression and anterior neural plate invagination, as in blebbistatin-treated embryos (Figures 4E and 4F; Movie S6), but without apical expansion of the posterior neural plate. Furthermore, quantitation of active myosin levels by immunofluorescence in H1152-treated embryos revealed a strong inhibition of myosin activation along Ne/Epi junctions ahead of the zipper relative to identically staged controls (Figure 4G), and live imaging confirmed a complete inhibition of junctional shortening (Movie S6; Figure S1H). Zippering also failed in embryos treated with a second ROCK inhibitor, Y-27632, consistent with a previous report (Ogura et al., 2011). However, this failure was accompanied by a strong disruption of Ne/Epi junctions, consistent with known off-target effects of Y-27632 (Atwood and Prehoda, 2009).

To further test a role for localized Rho/ROCK-dependent contractility in zippering, we expressed a dominant-negative form of RhoA downstream of the fucosyltransferase promoter (pFT::RhoA DN), using coexpressed GFP (pFT::GFP) to mark the domain of expression. We exploited mosaic expression of the electroporated transgenes (Zeller et al., 2006) to compare embryos with two distinct classes of expression pattern (Figure 4H, top). In class A, RhoA DN was expressed broadly in the left or right posterior epidermal cells, but not in the single rows of Ne and Epi cells flanking the Ne/Epi boundary. In class B, RhoA DN was expressed broadly in the left or right posterior epidermis, including the Ne and Epi cells flanking the Ne/Epi boundary. Control embryos expressing GFP in either pattern class closed the neural tube with high frequency (class A: 88%, n = 18; class B: 93%, n = 14; Figure 4, bottom). The majority of embryos (14/15; Movie S7) with class A RhoA DN expression underwent normal invagination and zippering. In contrast, 18/20 embryos with class B RhoA DN expression invaginated normally but failed to undergo zippering and neural tube closure. Significantly, in a small fraction of embryos, RhoA DN was expressed only in the

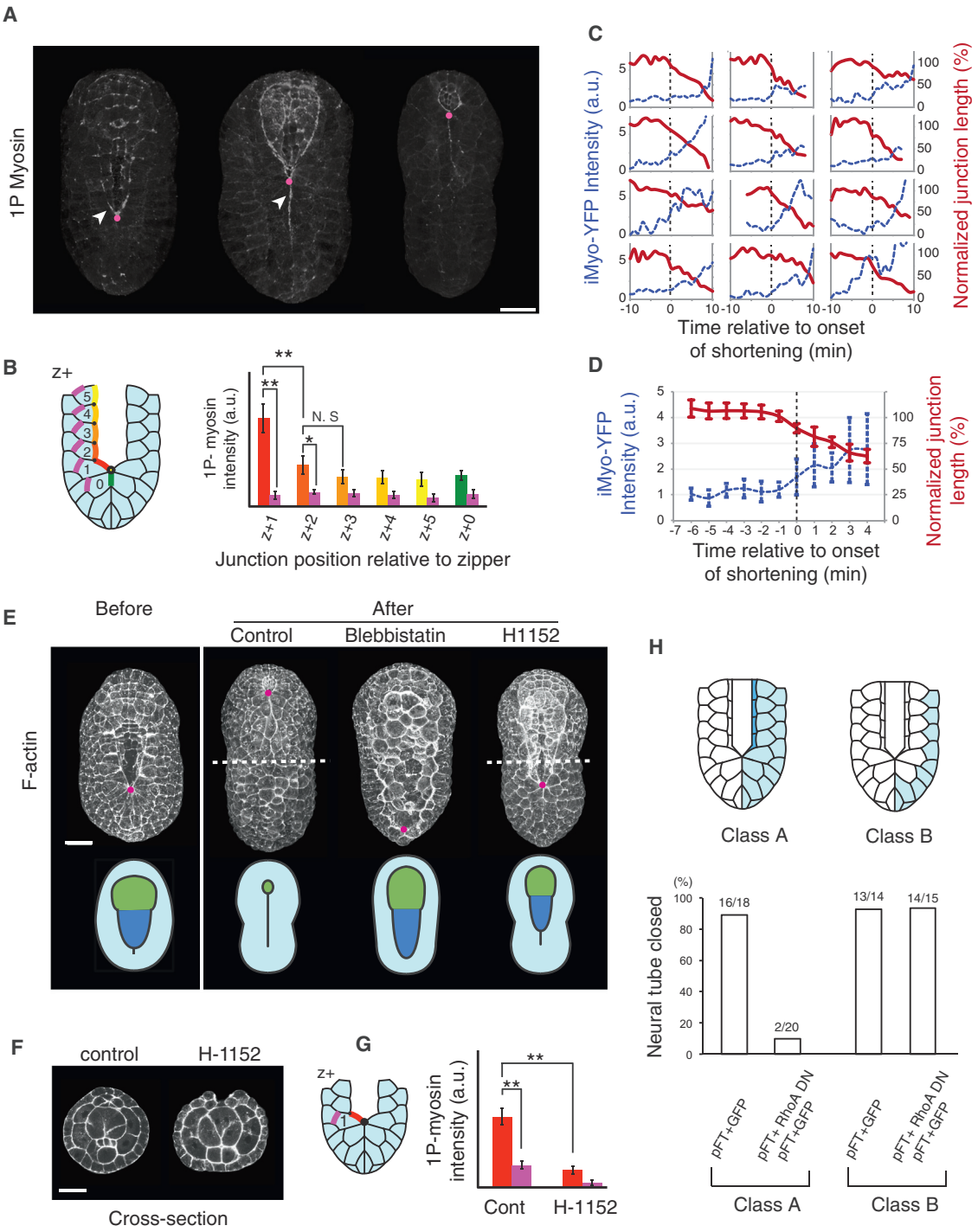

Figure 4. Junctional Contraction and Zipper Progression Require ROCK-Dependent Myosin Contractility

(A) Distribution of 1P myosin during zippering. 3D surface rendering of the dorsal surface of embryos at early (left), intermediate (middle), and late (right) zippering stages immunostained with anti-1P-myosin antibody. White arrowheads indicate increased myosin, ahead of (left) and behind (middle) the zipper.

(B) Relative 1P myosin intensity along different junctions whose positions are color-coded on the embryo schematic to the left as follows: Red-yellow is proximal-distal Ne/Epi junctional position relative to the zipper, green is new Epi/Epi junctions behind the zipper, and purple is the corresponding Epi/Epi control junction (n = 8 junctions for each measurement).

(C) Relationship between iMyo-YFP intensity and junctional length during individual junction shortening events in embryos electroporated with iMyo-YFP. Each panel represents a single junction contraction event. Red lines: normalized junction length. Blue dashed lines: relative iMyo-YFP fluorescence intensity averaged along the junction, excluding the vertices. We obtained similar results when vertices were included in the measurements (see Figure S1G). Vertical black dashed

(legend continued on next page)

single rows of cells flanking the Ne/Epi boundary, and these embryos always failed to zipper (n = 4; Movie S7). Thus, dominant-negative inhibition of RhoA along the Ne/Epi boundary on only one side of the embryo is sufficient to completely abrogate zippering and neural tube closure. Together, these results demonstrate that local activation of actomyosin contractility by the RhoA/ROCK pathway at Ne/Epi junctions is required for junctional contraction, zippering, and neural tube closure.

Laser Ablation Reveals a Close Correspondence between Myosin Activation and Junctional Tension

Our results thus far suggest that junction deformation and zipper progression are driven by differences in junctional tension patterned by differential activation of myosin. To test this more directly, we used laser ablation to estimate relative differences in junction tension (Rauzi et al., 2008; Fernandez-Gonzalez et al., 2009). We focused a nitrogen-pumped dye laser on individual junctions in embryos expressing ZO1-3xGFP and used several short pulses to mechanically disrupt the junction without killing the associated cells (see Experimental Procedures). The typical response to laser ablation was a rapid retraction of junctional material to the endpoints of the cut junction and a rapid movement of the junction endpoints away from the site of ablation, followed by a slower recovery of the junction toward its original precut length (Figures 5A, 5A′, and S2; Movie S8). As in previous studies (Rauzi et al., 2008), we took the initial velocities of vertices flanking the ablated junction as a relative measure of tension along the junction just before ablation (Figure 5B). We sampled estimates of junctional tension during zippering at different junction positions along the Ne/Epi boundary relative to the advancing zipper on newly formed junctions just behind the zipper and at more lateral Epi/Epi junctions. We observed a striking correspondence between estimates of relative tension, the measured distribution of active myosin, and the pattern of junctional shortening events. Junctional tensions were higher along the Ne/Epi boundary than in more lateral regions and highest just ahead of the advancing zipper (Figures 5C and S2). Interestingly, tensions were also high along newly formed Epi/Epi junctions behind the zipper, where myosin is also enriched (arrowhead in Figure 4B). Significantly, treatment with H1152 reduced tensions along Ne/Epi junctions just ahead of the zipper to below the levels on lateral Epi/Epi junctions in untreated controls (Figure 5C), suggesting that the increased tension is a specific consequence of local ROCK-dependent myosin II activation. In summary, we observe a very strong correlation between local myosin activation; elevated junction tension; and rapid, sequential junctional shortening along the Ne/Epi boundary during zippering.

Design of a Tension-Based Cytomechanical Model for Zippering

Our experimental observations suggest a working model for zippering and neural tube closure in which (1) sequential activation of Rho/ROCK-dependent actomyosin contractility just ahead of the zipper promotes an increase in junction tension that drives rapid junctional shortening to pull the zipper forward and draw the edges of the neural plate toward the midline, (2) resistance to zipper progression builds as cells behind the zipper become stretched away from their preferred isodiametric shapes, and (3) this resistance is dissipated by junction exchange and detachment of stretched cells from the zipper.

To test and elaborate this model, we turned to computer simulations, using previously developed methods and software (Sherrard et al., 2010). Details of model formulation and discussion of the model's assumptions can be found online (see Supplemental Experimental Procedures and Supplemental Modeling Procedures). An additional online supplement contains software and input files necessary to recreate many of the simulations (see Protocol). Briefly, we modeled the dorsal surface of a neurula-stage ascidian embryo as a 2D sheet of epidermal cells connected to one another along common junctions (Figure 6A). We modeled junctions as chains of discrete segments, connected through springs at vertices where three or more junctions meet. We endowed each segment with active contractility, characterized by a tension T and passive resistance to deformation, characterized by an effective viscosity μ_{eff}. On each model cell, we imposed a "pseudo-pressure" force that resists large changes in cell surface area, consistent with minimal variation in apical surface area during zippering in vivo. Finally, we represented the underlying neural tube/notochord and anterior brain as solid structures that resist medial bending and axial shortening (neural tube/notochord) or radial compression (anterior brain) with forces whose magnitudes are proportional to the degree of tissue strain. We ignored the small degree of axial extension (~10%) that occurs during zippering in vivo.

We used Newton's Laws to balance the active and passive forces on all segments and solved the resulting equations numerically to compute the deformations of cell boundaries over time. We allowed junctions to merge with the zipper whenever their lengths fell below a minimal value and modeled

line indicates the onset of shortening, defined as the time at which the junction first shortens past 90% of its preshortened plateau length (see Experimental Procedures for definition and measurement of plateau length).

(D) Distribution of iMyo-YFP averaged over 12 junctional shortening events. Data from individual junctions were aligned with respect to the onset of shortening. Legend is the same as in (C).

(E) Effects of drug treatment on zippering. Upper: embryos fixed and stained with phalloidin. The leftmost picture shows an embryo at start of drug treatment, then from left to right: control, 100 μM blebbistatin-treated and 1 μM H1152-treated embryos after treatment. Bottom: cartoons illustrating the extent of zippering in embryos shown in the upper panel. Green, brain; blue, nerve cord. Gray dashed lines indicate the cross-section position in control and H1152-treated embryos shown in (F).

(F) Cross-section along the AP axis of control (left) and H1152-treated (right) embryos shown in (E), with dorsal at the top.

(G) Relative 1P myosin intensity at Ne/Epi junction ahead of the zipper (red) and control junction (purple) in control and H1152-treated embryos (n = 10 each).

(H) Effect of misexpressing RhoA DN on neural tube closure. Top panels illustrate the two classes of expression pattern analyzed. Bottom graph quantifies successful zippering events in both classes, in embryos expressing pFT::GFP alone or pFT::GFP + pFT::RhoA DN. Magenta circles indicate zipper position. *$p < 0.05$, **$p < 0.002$, Student's t test. Error bars are SEM. Scale bars, 25 μm.

See also Figure S1.

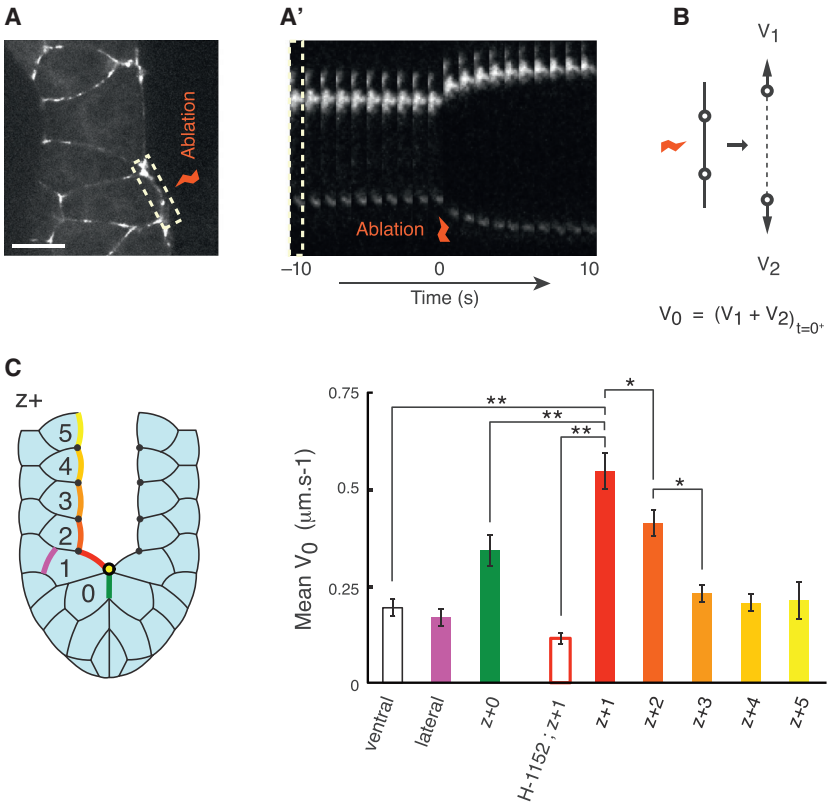

Figure 5. Distribution of Relative Tension at Cell-Cell Junctions Matches the Pattern of Active Myosin Accumulation

(A) Example of a laser ablation experiment, on Ne/Epi junction ahead of the zipper. White-dash box in (A) corresponds to leftmost stripe in (A′), and shows the ablated junction.

(A′) Kymograph of the time-lapse movies corresponding to (A) (Movie S8). Orange broken lines indicate the time point of ablation.

(B) Schematic of ablated junction. Circles indicate vertices. V_1 and V_2 represent vertices velocity.

(C) Left: color-scheme detailed on an embryo schematic. Red-yellow is proximal-distal Ne/Epi junction position relative to the zipper, green is new Epi/Epi junction behind the zipper, and purple is the corresponding Epi/Epi control junction. Right: initial velocity after ablation, as described in (B), in control and H1152-treated embryos. Colors in the graph correspond to the junction position in the schematic on the left. Bar outlined in red indicates z + 1 junction in H1152-treated embryos. Other bars correspond to control embryos. From left to right: n = 11 (ventral), 11 (lateral), 12 (z + 0), 11 (z + 1, H1152-treated), 14 (z + 1, control), 9 (z + 2), 7 (z + 3), 9 (z + 4), 6 (z + 5). *$p < 0.05$, **$p < 0.002$, Student's t test. Error bars are SEM. Scale bars, 5 μm.

See also Figure S2.

detachment of cells from the zipper as events that occur with a fixed delay (Figures S3A and S3B; see Supplemental Experimental Procedures and Supplemental Modeling Procedures).

Computer Simulations Support a Tension-Based Model for Zippering

We first asked whether simulations constrained by our experimental measurements could reproduce the observed kinematics of zippering. We assigned values for junction tensions to be the average relative values measured by laser ablation (Figure 5C), distinguishing primary Ne/Epi (one from zipper), secondary Ne/Epi (two from zipper), all other Ne/Epi, newly formed Epi/Epi, and all other Epi/Epi junctions (Figure 6A). We assigned the same baseline tension value to primary and secondary junctions. We then modeled the rapid contraction of primary junctions by setting their tensions to a higher primary level at a fixed time and allowing it to remain there until that junction merged with the zipper. We set the interval between primary contractions, and a fixed time before cell detachment from the zipper, to the average of measured values (Figures S3C and S3D). We assumed that effective viscosity was identical for all junctions, and we tuned its value such that the average shortening speed of primary junctions matched our measured values (Figure S3E).

With no further adjustment of model parameters, our simulations reproduced measured zippering speeds (Figures 6B and 6C; see Protocol). They also reproduced the average ratio of axial zipper advance to net shortening of axial junction length during individual contraction events (140% ± 29% in silico versus 126% ± 38% in vivo) and the characteristic sequence of cell stretching, detachment, and cell shape relaxation behind the zipper (Movie S9). The predicted zippering speed was insensitive to variation in initial cell shapes, to the magnitudes of forces that resist axial shortening and radial brain compression, and to the magnitudes of pseudo-pressure forces that resist changes in individual cell areas (Figures S3F–S3H). The predicted zippering speed was insensitive to forces resisting medial bending up to a threshold level, but above that level, zippering rapidly stalled (Figure S3I). These results both confirm that the simulated zippering mechanism can produce force to draw the neural folds together and reveal limits on that force. Thus, given the assumptions of our model, the measured variation in junctional tension, frequency of primary junction contractions, and rates of cell detachment are sufficient to explain the observed dynamics of zipper progression.

To gain further insights into the dynamics of zipper progression, we analyzed the balance of axial forces around primary junctions during simulated zippering (Figure 7A). We defined the primary contraction force to be the axial component of the contractile tension on primary junctions (red junctions and arrows in Figure 7A), the anterior tissue resistance to be the sum of all axial forces (excluding viscous forces) acting on the anterior endpoints of primary junctions (orange junctions and arrows in Figure 7A), and the posterior tissue resistance to be the sum of all axial forces (again excluding viscous forces) acting on the posterior endpoints (blue junctions and arrows in Figure 7A). Note that the tissue resistances depend both on junctional tension and orientation.

During each contraction cycle, these forces fluctuate as primary contractions drive the realignment of anterior and posterior

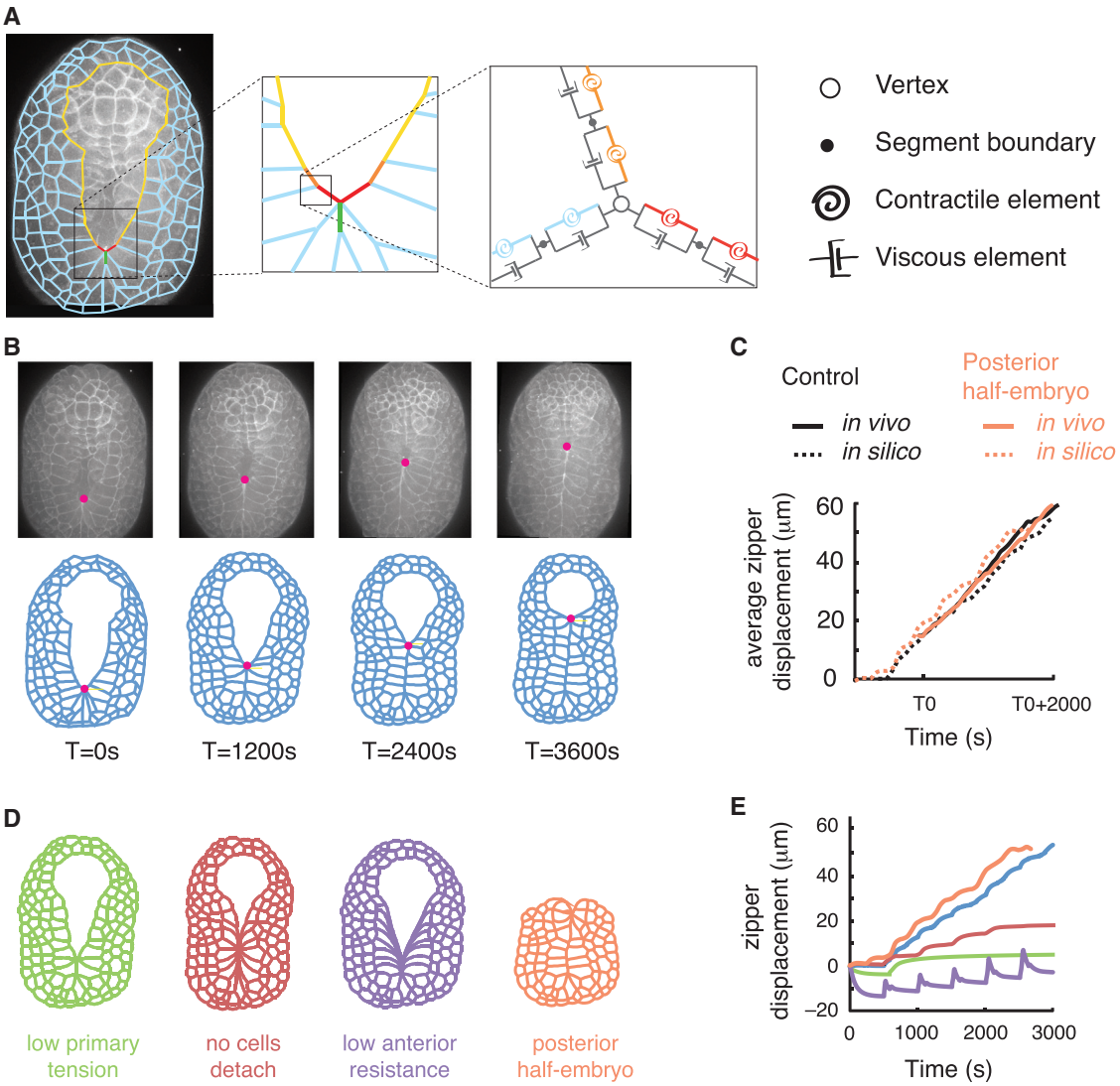

Figure 6. Simulations Based on Differences in Junctional Tension Reproduce Zippering

(A) Design of the simulation. Left: initial geometry of the simulation, color coding the different types of junctions defined in the simulation, overlaid with the corresponding micrograph. Middle: detailed view of the zipper region. Right: each model segment is composed of a viscoelastic element, defined by a single parameter across the simulation, and a contractile element, for which a value is specified for each junction type.

(B) Snapshots of zippering at T = 0, 1200, 2400, and 3600 s (from left to right), in vivo (top), and in silico (bottom) (see Movie S9). Solid magenta circles indicate the zipper positions.

(C) Comparison of zipper displacement in vivo and in silico, for control and posterior half-embryos, for reference parameters (in vivo, solid lines; in silico, dashed lines; control, black; posterior half-embryo, orange). For in vivo measurement, embryos expressing ZO1-3xGFP were imaged in time lapse and zipper position recorded over time.

(D and E) Comparison of simulation outcomes for different in silico perturbations (simulations are shown in Movie S10; see main text for details): green, low tension on primary junctions; red, no cell detachment behind the zipper; magenta, low anterior tissue resistance; orange, posterior half-embryos.

(D) Simulation snapshots show the outcome at T = 3600 s for each simulation (except posterior half-embryo shown at T = 2640 s).

(E) Plots of zipper displacement versus time for the different conditions shown in (D), with control simulation shown in blue. See also Figure S3.

junctions or as cells detach behind the zipper (Figure 7B). However, averaged over one contraction cycle, the primary contractile force dominated both anterior and posterior tissue resistance, and the anterior tissue resistance exceeded the posterior tissue resistance (Figures 7B and S4A). Reducing primary contractile force, increasing posterior resistance, or reducing anterior resistance beyond threshold values strongly reduced or abolished zippering (Figures 8A–8C and S4; see also Protocol). Thus, an anterior versus posterior imbalance of tissue resistance converts inherently symmetrical primary contractions into efficient unidirectional zipper progression. Reducing cell detachment rates behind the zipper below a threshold value lead to a buildup of posterior resistance and caused the zipper to stall, confirming an essential requirement for junctional exchange and cell detachment to maintain the imbalance of force that allows zipper progression (Figure 8D; see also Protocol).

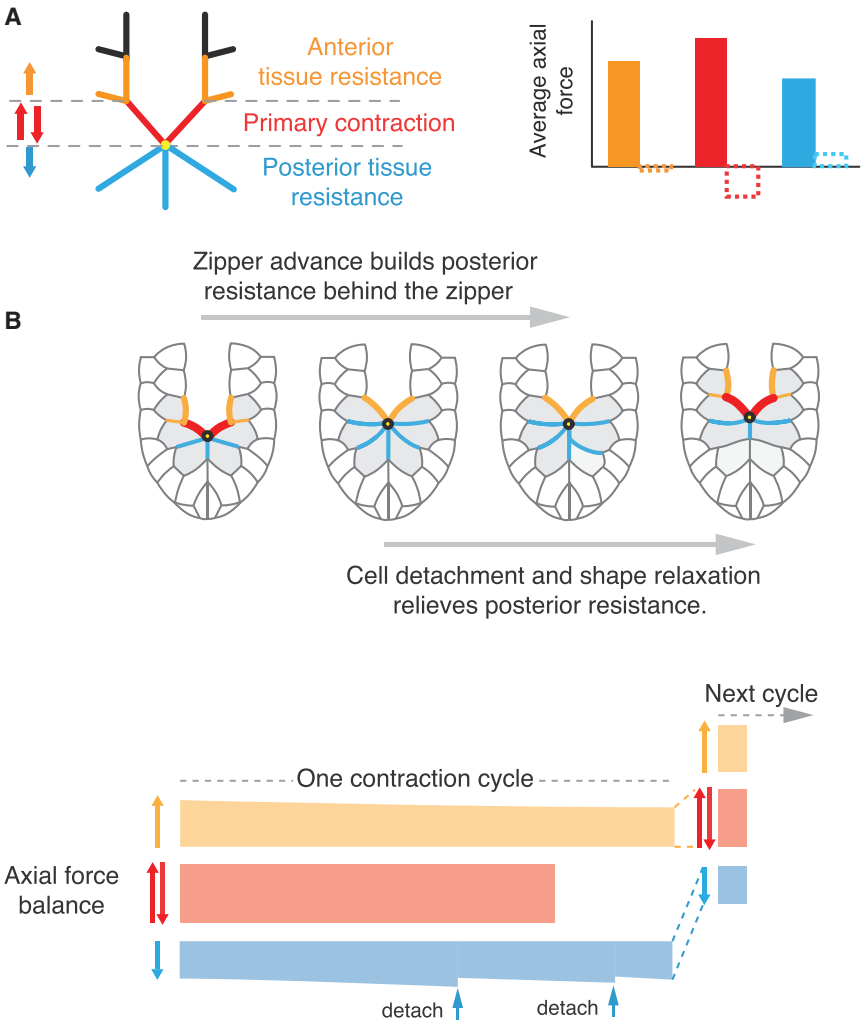

Figure 7. Force Balance during Contraction and Zipper Progression

(A) Left: schematic showing the relative contributions of primary contraction and anterior versus posterior tissue resistance to shortening of the primary junction and net forward movement of the zipper. Right: magnitude of active (solid) and passive (dashed) forces, averaged over the duration of a single simulation. Orange, anterior resistance; blue, posterior resistance; red, primary junction.

(B) Top: schematic view of one contraction cycle showing contraction of the primary junction combined with stretching and detachment of cells behind the zipper. Bottom: schematic view of the evolving force balance during one contraction cycle. Color code as in (A). See also Figure S4.

Interestingly, increasing primary contractile force, decreasing posterior resistance (by reducing posterior tension or detachment rates), or increasing anterior resistance beyond wild-type values produced little or no increase in zippering speed (Figures 8A–8D; see also Protocol). In contrast, reducing the average interval between primary contractions below the measured value produced a marked increase in zippering speed (Figure 8E). This suggests that the balance of force across primary junctions is not itself rate limiting for zipper progression in normal embryos; rather, it is primarily the frequency of contraction events that limits zipper speed.

To further test the model, we asked if simulations using wild-type parameters could reproduce the zippering dynamics observed in posterior half-embryos. Indeed, we found that in silico, as in vivo, zippering of posterior half-embryos proceeded at normal speeds relative to intact controls (Figures 6C–6E; Movie S10; see also Protocol). These results highlight a key difference between zippering by sequential contraction and a more widely studied mode of epithelial closure, which involves uniform contraction of a continuously tensioned supercellular actomyosin purse string (Martin and Parkhurst, 2004; Fernandez-Gonzalez and Zallen, 2013; Abreu-Blanco et al., 2012). In particular, they show that a continuously tensioned boundary is not required for zippering to proceed; instead, local tissue resistance is sufficient to support the imbalance of forces that drives zippering both in normal and in posterior half-embryos.

We hypothesized that sequential contraction might be more effective than uniform contraction at closing the neural tube because it would be less sensitive to external forces (e.g., within the underlying notochord) that resist axial shortening and/or drive axial extension at the same time that zippering occurs (Munro and Odell, 2002; Munro et al., 2006). To test this, we compared sequential contraction with a scenario in which all junctions along the Ne/Epi boundary contract with the same tension as the primary junction. We fixed all other parameters at wild-type values except for the forces that resist axial shortening, which we varied systematically. Strikingly, we found that sequential contraction produced significantly faster zippering than uniform contraction over the entire range of axial resistance values (Figure 8F and Movie S11; see also Protocol). Furthermore, the amount of axial resistance required to prevent axial shortening during closure was significantly greater for the uniform contraction scenario (Figure 8G), and the uniform contraction mechanism was severely compromised by this level of resistance, whereas the sequential contraction mechanism was not (Figure 8F). Thus, all other things equal, zippering by sequential contraction is significantly faster and less sensitive to axial extension than uniform contraction.

Finally, we asked whether the zippering mechanism documented here could plausibly contribute to neural tube closure in larger vertebrate embryos with many more cells. To this end, we compared simulated zippering in two model embryos with idealized geometries, one a 5-fold ''photographic enlargement'' of the other, containing 5-fold more cells in both axial and perpendicular directions (Movie S12; see also Protocol). We set all other model parameters to identical reference values

except for the stiffness parameter that governs the strength of medial resistance, which we varied identically for both cases. We found that for low levels of medial resistance, zippering proceeded at the same speed for both scenarios (Figures 8H–8K). In both cases, zippering could overcome medial resistance to draw the "neural folds" together, although zippering stalled at ~2-fold lower levels of medial resistance in the larger embryos (Figure 8K). We conclude that the sequential contraction mechanism described here could contribute to zippering and neural tube closure in much larger embryos.

DISCUSSION

Unidirectional zippering is a universal feature of neural tube closure in chordates, but what drives zippering and determines its direction and speed remains unclear. Here, we have identified the cytomechanical basis for zippering and neural tube closure in a simple model chordate. We have shown that zipper progression is coordinated and driven by a wave of elevated Rho/ROCK-dependent actomyosin contractility that proceeds from posterior to anterior along the Ne/Epi boundary just ahead of the advancing zipper. Local activation of myosin promotes a transient increase in junctional tension and rapid shortening of Ne/Epi junctions just ahead of the zipper, driving the zipper forward and drawing pairs of Ne/Epi cells to the midline to initiate the process of junction exchange. During junctional exchange, these cells stretch transiently, resisting forward movement of the zipper, before detaching and relaxing to more isodiametric shapes. Our computer simulations show that measured differences in junctional tension, together with the measured time interval between contractions of primary junction and the measured time delay between the end of contraction and cell detachment, are sufficient to explain the observed kinematics of zipper progression.

Together, our observations reveal how a dynamical interplay of local junctional contraction, exchange, and cell detachment leads to efficient unidirectional zipper progression (Figure 7B). During the contraction of each primary junction, the recruitment and realignment of junctions behind the zipper produce a transient increase in net posterior tissue resistance. Absent junctional exchange and cell detachment, this resistance would build until the zipper stalls (Figures 6D–6E and S4; Movie S10). Normally, however, the detachment of cells behind the zipper relieves this resistance at the average rate of one detachment event per junction contraction. This yields, on average, a small imbalance of anterior versus posterior tissue resistance that is sufficient to convert the inherently symmetrical contractions of the primary junction into net forward movement. Thus, a sequence of rapid junction shortening events is rectified by junctional exchange and cell detachment into continuous and irreversible zipper progression. Interestingly, varying model parameters with respect to wild-type values suggest that neither the strength of primary contractions, rates of cell detachment, nor tension on junctions behind the zipper is rate limiting for zipper progression in normal embryos. Thus, zippering appears to operate in a regime where it is buffered against variation in these properties.

Our results highlight key differences between zippering by sequential contraction and a more commonly studied mode of epithelial closure in which uniform contraction of a continuously tensioned actomyosin purse string drives uniform shortening of an entire boundary (Martin and Parkhurst, 2004; Osterfield et al., 2013; Fernandez-Gonzalez and Zallen, 2013; Abreu-Blanco et al., 2012). Our analysis of posterior half-embryos shows that zippering does not require a continuously tensioned boundary; instead, the force imbalance that drives each cycle of junction contraction and zipper progression is largely sustained by local resistance of nearby cells to deformation.

A direct comparison in silico suggests that both mechanisms could accomplish neural tube closure in ascidians, but sequential contraction works better for two reasons: First, during sequential contraction, junctional shortening, exchange, and cell detachment are tightly coupled at a single locus—the moving zipper. Thus, resistance built during each cycle of junction contraction is rapidly dissipated such that the additional force required for the next cycle to complete remains small. In contrast, when deformation is distributed throughout a uniformly tensioned boundary, it takes longer for any individual junction to shrink to a point where junctional exchange, and dissipation of tissue resistance, can occur. Second, during sequential contraction, the deformations are highly localized, while a uniform contraction mechanism requires significant global deformation of surrounding tissues. This implies that a sequential contraction mechanism should be far less sensitive to global mechanical context than uniform contraction. In particular, zippering coincides with active elongation of the underlying notochord and neural tube, to which the zippering cells are tightly attached. Our simulations show that a uniform contraction mechanism is severely compromised by a level of external force sufficient to prevent axial shortening during zippering, while the sequential mechanism is not (Figures 8F and 8G; Movie S11). Thus, zippering by sequential contraction may be particularly favored in tissues undergoing axial extension. Interestingly, the ascidian embryo uses sequential contraction to close the elongating axial nerve tube but appears to use a global purse string contraction to close the anterior brain, which does not undergo axial elongation (Figure 1B; Movie S1; F.B.R., H.H., and E.M.M., unpublished data).

To what extent could the zippering mechanism identified here contribute to zippering and neural tube closure in larger vertebrate embryos? Our simple simulations suggest that, all other things equal, zippering by sequential contraction could work in a much larger embryo. In vertebrates, multiple mechanisms contribute force to bring the neural folds together, including bending of the neural plate about the midline and lateral hinge points (Haigo et al., 2003; Hildebrand 2005); convergent extension of the neural plate (Wallingford and Harland, 2002; Nishimura et al., 2012); and, possibly, active spreading of the lateral epidermis (reviewed in Colas and Schoenwolf, 2001). The sequential contraction mechanism we describe here would act in addition to these others by producing forces that assist in bringing the folds together. It could also help to consolidate or rectify work done by these other mechanisms by facilitating local junctional exchange and cell detachment behind the zipper. Interestingly, recent work suggests that localized junctional shortening accompanies zippering during dorsal closure in *Drosophila* embryos, suggesting that a sequential contraction mechanism may contribute to zipper progression in that context as well (Peralta et al., 2008).

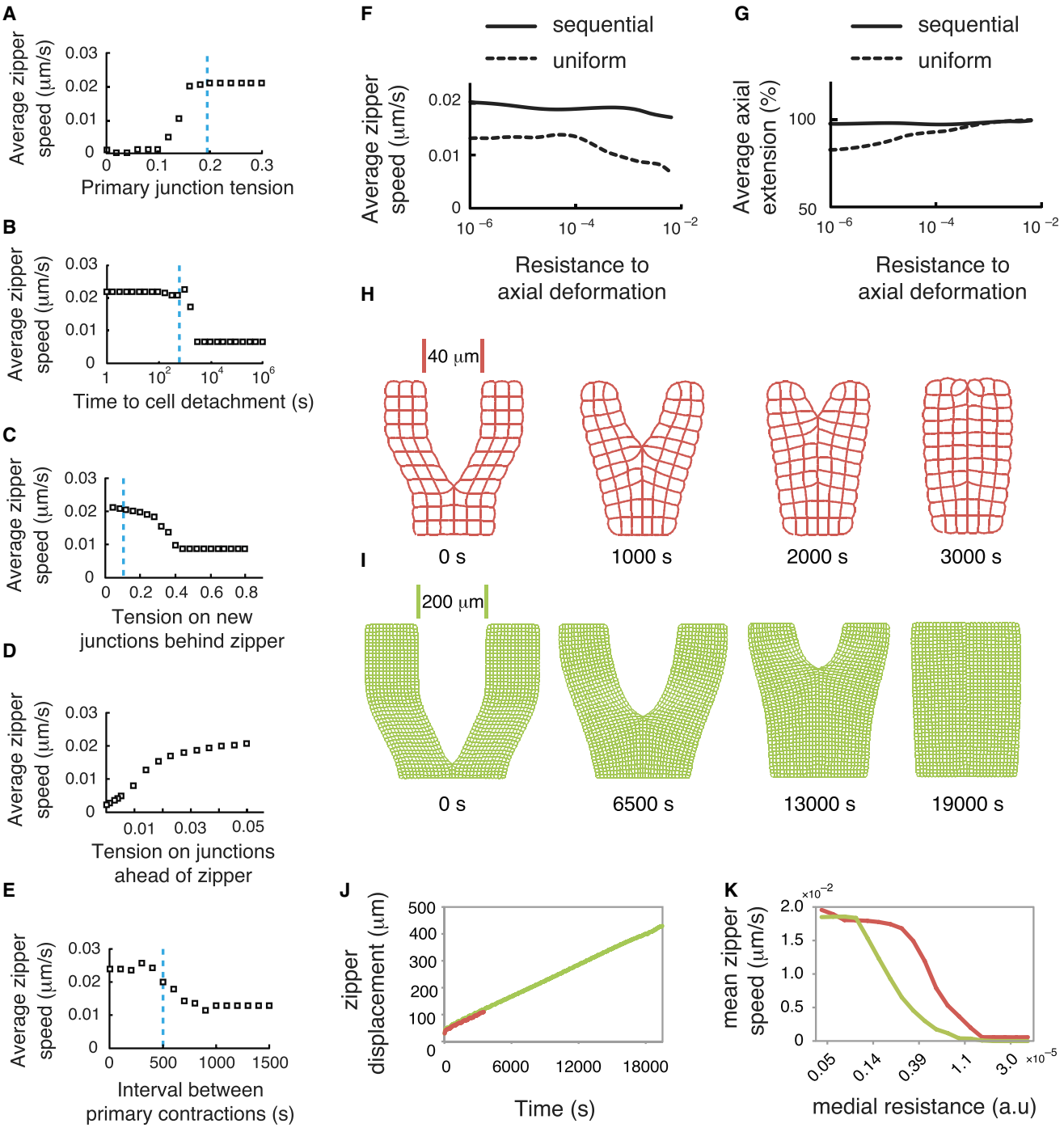

Figure 8. Key Determinants of Zippering Speed

(A–E) Dependence of zipper speed on different model parameters: (A) primary junction contraction force; (B) time lag between the end of a primary contraction event and detachment of that cell from the zipper (the average value measured in vivo is 588 s; see Figure S3C); (C) tension on newly formed junctions behind the zipper; (D) anterior tissue resistance, which was varied by assigning a single tension level to all Ne/Epi junctions ahead of the zipper and all Epi/Epi junctions connected to the Ne/Epi boundary, and then varying this single tension value; and (E) interval between consecutive contraction events (the average value measured in vivo is 504 s; see Figure S3D). Vertical dashed blue lines in (A), (B), (C), and (E) indicate the parameter measured experimentally in vivo and used as a reference value in simulations.

(F and G) Comparison of zippering with uniform versus sequential modes of junctional contraction and its dependence on axial resistance to deformation (see Movie S11).

(F) Average zipper speed for a range of values of the axial stiffness comparing sequential (solid black line) and uniform (dashed black line) contraction.

(G) Average axial extension for a range of values of the axial stiffness comparing sequential (solid black line) and uniform (dashed black line) contraction.

(H–K) Dependence of zippering speed on tissue size (see Movie S12).

(legend continued on next page)

Our data suggest that local differences in junctional tension are sufficient to explain the speed and direction of zipper progression in ascidian embryos, but other mechanisms may also contribute, both in ascidians and in higher vertebrates. For example, Pyrgaki et al. (2010) recently described a novel cellular mechanism for neural tube closure in mouse embryonic midbrain known as "buttoning," in which numerous thin filopodia processes extend between opposing folds to establish nascent cell-cell contacts at multiple independent closure sites, followed by zipping between these sites. Similar processes have been observed during zippering closure, both in mouse (Massarwa and Niswander, 2013) and ascidian (Ogura et al., 2011) embryos, as well as during dorsal closure in *Drosophila* (Jacinto et al., 2000). Whether they produce forces to assist in closure, mediate signals that coordinate force production by other mechanisms (such as actomyosin contractility), or both, remains to be seen.

Our work identifies spatiotemporal patterning of myosin activation at the Ne/Epi boundary as a key point of embryonic control over zippering. Recent work suggests that differential expression of junctional transmembrane proteins including Crumbs, Notch/Delta, and Echinoid, a nectin homolog, across tissue boundaries plays a key role in localizing myosin activation to those boundaries (Major and Irvine, 2006; Laplante and Nilson, 2011; Röper, 2012). It will be interesting to determine whether homologs of these proteins are involved in controlling myosin localization during zipper progression in ascidians.

What produces a posterior-to-anterior wave of activation remains to be determined. An attractive scenario is that the zipper produces one or more activating signals whose range extends with the zipper as it moves or that propagate along the boundary, e.g., through tension-dependent activation of myosin II (Pouille et al., 2009; Fernandez-Gonzalez et al., 2009; Farge, 2011). Identifying these signals and characterizing how they propagate will be an interesting topic for future work.

Finally, our work highlights the central importance of junctional remodeling and exchange for both zipper advance and for the fusion/separation of neural tube and epidermis. Junctional remodeling during cell neighbor exchange is likely to be a tightly regulated process, probably involving a combination of general mechanisms (Blankenship et al., 2006; Bardet et al., 2013) and the specific interactions between cells based on their differing identities (Maître et al., 2012), but how it is controlled by tissue-specific inputs, local tensions, and other factors remains poorly understood in any system. Zippering in ascidians will be a useful model for exploring these questions because junctional remodeling and exchange are confined to a single well-defined locus.

EXPERIMENTAL PROCEDURES

Embryo Culture and Manipulation

Ciona intestinalis adults were collected and shipped from Half Moon Bay, Oyster Point, and San Diego (M-Rep), and then maintained in oxygenated sea water at ~16°C. We used standard methods for embryo culture, electroporation, drug treatment, and microsurgery (Sherrard et al., 2010; Corbo et al., 1997; Bertrand et al., 2003; Hotta et al., 2007; see Supplemental Experimental Procedures for details).

Immunostaining and Quantitative Analysis of F-Actin and Phosphomyosin Distributions

We fixed and stained embryos for F-actin and phosphomyosin as described previously (Sherrard et al., 2010) and then imaged them on a Zeiss LSM 510 confocal microscope with a 40x/1.3NA (numerical aperture) oil-immersion objective. We performed image processing and measurements of junctional intensity manually in ImageJ (http://rsbweb.nih.gov/ij/). Please see Supplemental Experimental Procedures for details).

Tissue-Specific Expression of FP Fusions

Constructs for tissue-specific expression of GFP and YFP fusions using previously characterized pFOG and pFT promotors (Pasini et al., 2006; Roure et al., 2007; Pasini et al., 2012) were produced using standard Gateway cloning (Invitrogen), as described previously (Roure et al., 2007; see Supplemental Experimental Procedures for details).

4D Time-Lapse Imaging

We acquired time-lapse sequences of 3D image stacks using a Nikon ECLIPSE-Ti inverted microscope equipped with 20x and 60x water-immersion lenses, solid-state 50 mW 481 and 561 laser excitation, a Yokogawa CSU-X1 spinning disk scan head, a Rolera em-c^2 EM-CCD camera, and a motorized stage with piezoelectric z-axis control (see Supplemental Experimental Procedures for details).

Laser Ablations

We performed laser ablations using a MicroPoint nitrogen-pumped dye laser (Andor Technologies), tuned to excite at 435 nm and focused through a 60x/1.2NA water-immersion objective to a diffraction-limited spot in the image plane. We ablated individual junctions in embryos expressing ZO1::GFP using ~7 pulses at 15 Hz with 50% attenuation, yielding ~175 μJ total energy. The typical response was an initial lesion followed by rapid expansion of the cut and then a slower wound-healing response over several minutes (see Figure S2; Movie S8), after which the ablated junction and flanking cells participated normally in subsequent events (data not shown). To monitor the response, we collected images at 1 s intervals before, during, and after the ablation and tracked the vertices at both ends of the cut junction manually using ImageJ. Following previous studies (Rauzi et al., 2008), we took the initial speed of separation of the junction endpoints (see Figures 5A and 5B) to be proportional to the tension on the junction prior to ablation, assuming that the local viscosity is homogeneous throughout the tissue.

Morphometric Measurements

We performed all measurements on time-lapse sequences acquired at 10 s intervals from embryos expressing ZO1-3xGFP. Each frame was the maximum intensity projection of 11 images collected at 0.75 μm steps in z near the apical surface. We only analyzed movies in which zippering was less than 25% complete at the beginning and proceeded to completion. We measured junction lengths, cell perimeter and area, and zipper vertex positions manually using ImageJ.

To identify the beginning of each primary contraction, we smoothed the junction length data using a ten-frame moving average, and then we determined the time point at which shortening speed increased above a threshold level. We took the end of the contraction to be the time point at which the junction length decreased below a minimal value. We measured the average contraction speed as the net change in length from beginning to end divided

(H) Snapshots from a simulation using in an idealized epidermis with identical rules, parameter values, and roughly the same number of cells as in the ascidian-specific simulations.

(I) Snapshots from a simulation representing a photographic enlargement of the embryo in (H) by a factor of 5, but with the same cell size and simulation parameters.

(J) Plots of zipper displacement versus time showing that zippering speed is nearly identical for the two simulations when the medial resistance is 0.

(K) Plots of zippering speed versus medial resistance for the two simulations. Zippering stalls at ~2.5-fold lower level of tissue resistance in the 5x embryos.

by the elapsed time. To compute the ratio of axial zipper advance to change in axial junction length during each primary contraction, we projected the net change in length and zipper displacement onto an axis defined by the initial and final positions of the zipper vertex. We measured the interval between primary contractions (Figure S3C) as the time between the beginnings of two consecutive contractions. We measured the time to detach from the zipper (Figure S3C) as the interval between the end of a contraction, determined as above, and the time at which we first detected relaxation of the cell that had contained that junction. Finally, to measure the average zipper speed in a given embryo, we identified time points near the beginning (less than 25% complete) and at the end of zippering, then divided the net displacement of the zipper vertex between these time points by the elapsed time.

Measurements of iMyo-YFP Intensity versus Junction Length

We measured junction lengths and iMyo-YFP intensities from time-lapse movies taken at 1 min intervals to avoid excessive photobleaching. Each frame was the maximum intensity projection of 15 images collected at 0.75 μm steps in z. We measured junction lengths as described above for Z01-3xGFP expressing embryos. We measured junctional iMyo-YFP intensities in ImageJ as mean gray levels averaged over 10 μm thick lines drawn along the junction of interest, and we aligned data from multiple junctions (Figure 4D) with respect to the onset of junction contraction (see Supplemental Experimental Procedures for details).

Computer Simulations

We performed all computer simulations using an extension of methods and software described in Sherrard et al. (2010). See Supplemental Experimental Procedures and Supplemental Modeling Procedures for details.

SUPPLEMENTAL INFORMATION

Supplemental Information includes Supplemental Experimental Procedures, Supplemental Modeling Procedures, four figures, and twelve movies and can be found with this article online at http://dx.doi.org/10.1016/j.devcel.2014.12.017.

AUTHOR CONTRIBUTIONS

F.B.R., E.M.M., H.H., and K.M.S. conceived the project. H.H. and F.B.R. performed and, with E.M.M., analyzed the embryological experiments. E.M.M. and H.H. performed and, with F.B.R., analyzed the numerical simulations. H.H., F.B.R., and E.M.M. wrote the article.

ACKNOWLEDGMENTS

This research was supported by a grant from the Edwin J. Mallinckrodt foundation (PI: E.M.M.) and by an NIH ARRA supplementary grant P50-GM066050-05S2 (PI: Garry Odell). We gratefully acknowledge members of the 2008 Dynamics of Cellular Morphogenesis Research Apprenticeship course—Brooke Danaher, Wei Deng, Sagar Joshi, Monica Montgomery, Shelby Simon, David Velásquez-Carvajal, and Diana White—for their contributions to the initial stages of this project. We thank Michelle Herko for technical support; Frank Perez, Agnès Roure, Sébastien Darras, Ute Rothbächer, Patrick Lemaire, Marion Guéroult Bellone, and Sabrina Hettinger for kindly providing constructs; and Victoria Foe, Garry Odell, and Guillaume Halet for useful discussions.

Received: February 4, 2014
Revised: November 7, 2014
Accepted: December 21, 2014
Published: January 26, 2015

REFERENCES

Abreu-Blanco, M.T., Verboon, J.M., Liu, R., Watts, J.J., and Parkhurst, S.M. (2012). Drosophila embryos close epithelial wounds using a combination of cellular protrusions and an actomyosin purse string. J. Cell Sci. *125*, 5984–5997.

Alvarez, I.S., and Schoenwolf, G.C. (1992). Expansion of surface epithelium provides the major extrinsic force for bending of the neural plate. J. Exp. Zool. *261*, 340–348.

Atwood, S.X., and Prehoda, K.E. (2009). aPKC phosphorylates Miranda to polarize fate determinants during neuroblast asymmetric cell division. Curr. Biol. *19*, 723–729.

Bardet, P.-L., Guirao, B., Paoletti, C., Serman, F., Léopold, V., Bosveld, F., Goya, Y., Mirouse, V., Graner, F., and Bellaïche, Y. (2013). PTEN controls junction lengthening and stability during cell rearrangement in epithelial tissue. Dev. Cell *25*, 534–546.

Bertrand, V., Hudson, C., Caillol, D., Popovici, C., and Lemaire, P. (2003). Neural tissue in ascidian embryos is induced by FGF9/16/20, acting via a combination of maternal GATA and Ets transcription factors. Cell *115*, 615–627.

Blankenship, J.T., Backovic, S.T., Sanny, J.S.P., Weitz, O., and Zallen, J.A. (2006). Multicellular rosette formation links planar cell polarity to tissue morphogenesis. Dev. Cell *11*, 459–470.

Bronner-Fraser, M., Wolf, J.J., and Murray, B.A. (1992). Effects of antibodies against N-cadherin and N-CAM on the cranial neural crest and neural tube. Dev. Biol. *153*, 291–301.

Camerer, E., Barker, A., Duong, D.N., Ganesan, R., Kataoka, H., Cornelissen, I., Darragh, M.R., Hussain, A., Zheng, Y.-W., Srinivasan, Y., et al. (2010). Local protease signaling contributes to neural tube closure in the mouse embryo. Dev. Cell *18*, 25–38.

Chaigne, A., Campillo, C., Gov, N.S., Voituriez, R., Azoury, J., Umaña-Diaz, C., Almonacid, M., Queguiner, I., Nassoy, P., Sykes, C., et al. (2013). A soft cortex is essential for asymmetric spindle positioning in mouse oocytes. Nat. Cell Biol. *15*, 958–966.

Colas, J.F., and Schoenwolf, G.C. (2001). Towards a cellular and molecular understanding of neurulation. Dev. Dyn. *221*, 117–145.

Copp, A.J., and Greene, N.D.E. (2010). Genetics and development of neural tube defects. J. Pathol. *220*, 217–230.

Copp, A.J., Stanier, P., and Greene, N.D.E. (2013). Neural tube defects: recent advances, unsolved questions, and controversies. Lancet Neurol. *12*, 799–810.

Corbo, J.C., Erives, A., Di Gregorio, A., Chang, A., and Levine, M. (1997). Dorsoventral patterning of the vertebrate neural tube is conserved in a protochordate. Development *124*, 2335–2344.

Farge, E. (2011). Mechanotransduction in development. Curr. Top. Dev. Biol. *95*, 243–265.

Fernandez-Gonzalez, R., and Zallen, J.A. (2013). Wounded cells drive rapid epidermal repair in the early Drosophila embryo. Mol. Biol. Cell *24*, 3227–3237.

Fernandez-Gonzalez, R., Simoes, S. de M., Röper, J.-C., Eaton, S., and Zallen, J.A. (2009). Myosin II dynamics are regulated by tension in intercalating cells. Dev. Cell *17*, 736–743.

Guillot, C., and Lecuit, T. (2013). Mechanics of epithelial tissue homeostasis and morphogenesis. Science *340*, 1185–1189.

Haigo, S.L., Hildebrand, J.D., Harland, R.M., and Wallingford, J.B. (2003). Shroom induces apical constriction and is required for hingepoint formation during neural tube closure. Curr. Biol. *13*, 2125–2137.

Hatta, K., and Takeichi, M. (1986). Expression of N-cadherin adhesion molecules associated with early morphogenetic events in chick development. Nature *320*, 447–449.

Hildebrand, J.D. (2005). Shroom regulates epithelial cell shape via the apical positioning of an actomyosin network. J. Cell Sci. *118*, 5191–5203.

Hildebrand, J.D., and Soriano, P. (1999). Shroom, a PDZ domain-containing actin-binding protein, is required for neural tube morphogenesis in mice. Cell *99*, 485–497.

Holmberg, J., Clarke, D.L., and Frisén, J. (2000). Regulation of repulsion versus adhesion by different splice forms of an Eph receptor. Nature *408*, 203–206.

Hotta, K., Mitsuhara, K., Takahashi, H., Inaba, K., Oka, K., Gojobori, T., and Ikeo, K. (2007). A web-based interactive developmental table for the ascidian Ciona intestinalis, including 3D real-image embryo reconstructions: I. From fertilized egg to hatching larva. Dev. Dyn. *236*, 1790–1805.

Ikenoya, M., Hidaka, H., Hosoya, T., Suzuki, M., Yamamoto, N., and Sasaki, Y. (2002). Inhibition of rho-kinase-induced myristoylated alanine-rich C kinase substrate (MARCKS) phosphorylation in human neuronal cells by H-1152, a novel and specific Rho-kinase inhibitor. J. Neurochem. *81*, 9–16.

Jacinto, A., Wood, W., Balayo, T., Turmaine, M., Martinez-Arias, A., and Martin, P. (2000). Dynamic actin-based epithelial adhesion and cell matching during Drosophila dorsal closure. Curr. Biol. *10*, 1420–1426.

Jaskoll, T., Greenberg, G., and Melnick, M. (1991). Neural tube and neural crest: a new view with time-lapse high-definition photomicroscopy. Am. J. Med. Genet. *41*, 333–345.

Komatsu, S., and Ikebe, M. (2004). ZIP kinase is responsible for the phosphorylation of myosin II and necessary for cell motility in mammalian fibroblasts. J. Cell Biol. *165*, 243–254.

Laplante, C., and Nilson, L.A. (2011). Asymmetric distribution of Echinoid defines the epidermal leading edge during Drosophila dorsal closure. J. Cell Biol. *192*, 335–348.

Maître, J.-L., Berthoumieux, H., Krens, S.F.G., Salbreux, G., Jülicher, F., Paluch, E., and Heisenberg, C.-P. (2012). Adhesion functions in cell sorting by mechanically coupling the cortices of adhering cells. Science *338*, 253–256.

Major, R.J., and Irvine, K.D. (2006). Localization and requirement for Myosin II at the dorsal-ventral compartment boundary of the Drosophila wing. Dev. Dyn. *235*, 3051–3058.

Marlow, F., Topczewski, J., Sepich, D., and Solnica-Krezel, L. (2002). Zebrafish Rho kinase 2 acts downstream of Wnt11 to mediate cell polarity and effective convergence and extension movements. Curr. Biol. *12*, 876–884.

Martin, P., and Parkhurst, S.M. (2004). Parallels between tissue repair and embryo morphogenesis. Development *131*, 3021–3034.

Massarwa, R., and Niswander, L. (2013). In toto live imaging of mouse morphogenesis and new insights into neural tube closure. Development *140*, 226–236.

Matsumura, F. (2005). Regulation of myosin II during cytokinesis in higher eukaryotes. Trends Cell Biol. *15*, 371–377.

Morita, H., Kajiura-Kobayashi, H., Takagi, C., Yamamoto, T.S., Nonaka, S., and Ueno, N. (2012). Cell movements of the deep layer of non-neural ectoderm underlie complete neural tube closure in Xenopus. Development *139*, 1417–1426.

Munro, E.M., and Odell, G.M. (2002). Polarized basolateral cell motility underlies invagination and convergent extension of the ascidian notochord. Development *129*, 13–24.

Munro, E., Robin, F., and Lemaire, P. (2006). Cellular morphogenesis in ascidians: how to shape a simple tadpole. Curr. Opin. Genet. Dev. *16*, 399–405.

Nicol, D., and Meinertzhagen, I.A. (1988a). Development of the central nervous system of the larva of the ascidian, Ciona intestinalis L. I. The early lineages of the neural plate. Dev. Biol. *130*, 721–736.

Nicol, D., and Meinertzhagen, I.A. (1988b). Development of the central nervous system of the larva of the ascidian, Ciona intestinalis L. II. Neural plate morphogenesis and cell lineages during neurulation. Dev. Biol. *130*, 737–766.

Nishida, H. (1987). Cell lineage analysis in ascidian embryos by intracellular injection of a tracer enzyme. III. Up to the tissue restricted stage. Dev. Biol. *121*, 526–541.

Nishimura, T., and Takeichi, M. (2008). Shroom3-mediated recruitment of Rho kinases to the apical cell junctions regulates epithelial and neuroepithelial planar remodeling. Development *135*, 1493–1502.

Nishimura, T., Honda, H., and Takeichi, M. (2012). Planar cell polarity links axes of spatial dynamics in neural-tube closure. Cell *149*, 1084–1097.

Nizak, C., Martin-Lluesma, S., Moutel, S., Roux, A., Kreis, T.E., Goud, B., and Perez, F. (2003). Recombinant antibodies against subcellular fractions used to track endogenous Golgi protein dynamics in vivo. Traffic *4*, 739–753.

Ogura, Y., Sakaue-Sawano, A., Nakagawa, M., Satoh, N., Miyawaki, A., and Sasakura, Y. (2011). Coordination of mitosis and morphogenesis: role of a prolonged G2 phase during chordate neurulation. Development *138*, 577–587.

Osterfield, M., Du, X., Schüpbach, T., Wieschaus, E., and Shvartsman, S.Y. (2013). Three-dimensional epithelial morphogenesis in the developing Drosophila egg. Dev. Cell *24*, 400–410.

Pai, Y.-J., Abdullah, N.L., Mohd-Zin, S.W., Mohammed, R.S., Rolo, A., Greene, N.D.E., Abdul-Aziz, N.M., and Copp, A.J. (2012). Epithelial fusion during neural tube morphogenesis. Birth Defects Res. A Clin. Mol. Teratol. *94*, 817–823.

Pasini, A., Amiel, A., Rothbächer, U., Roure, A., Lemaire, P., and Darras, S. (2006). Formation of the ascidian epidermal sensory neurons: insights into the origin of the chordate peripheral nervous system. PLoS Biol. *4*, e225.

Pasini, A., Manenti, R., Rothbächer, U., and Lemaire, P. (2012). Antagonizing retinoic acid and FGF/MAPK pathways control posterior body patterning in the invertebrate chordate Ciona intestinalis. PLoS ONE *7*, e46193.

Peralta, X.G., Toyama, Y., Kiehart, D.P., and Edwards, G.S. (2008). Emergent properties during dorsal closure in Drosophila morphogenesis. Phys. Biol. *5*, 015004.

Pouille, P.-A., Ahmadi, P., Brunet, A.-C., and Farge, E. (2009). Mechanical signals trigger Myosin II redistribution and mesoderm invagination in Drosophila embryos. Sci. Signal. *2*, ra16.

Pyrgaki, C., Trainor, P., Hadjantonakis, A.-K., and Niswander, L. (2010). Dynamic imaging of mammalian neural tube closure. Dev. Biol. *344*, 941–947.

Rauzi, M., Verant, P., Lecuit, T., and Lenne, P.-F. (2008). Nature and anisotropy of cortical forces orienting Drosophila tissue morphogenesis. Nat. Cell Biol. *10*, 1401–1410.

Ray, H.J., and Niswander, L. (2012). Mechanisms of tissue fusion during development. Development *139*, 1701–1711.

Röper, K. (2012). Anisotropy of Crumbs and aPKC drives myosin cable assembly during tube formation. Dev. Cell *23*, 939–953.

Roure, A., Rothbächer, U., Robin, F., Kalmar, E., Ferone, G., Lamy, C., Missero, C., Mueller, F., and Lemaire, P. (2007). A multicassette Gateway vector set for high throughput and comparative analyses in ciona and vertebrate embryos. PLoS ONE *2*, e916.

Sausedo, R.A., Smith, J.L., and Schoenwolf, G.C. (1997). Role of nonrandomly oriented cell division in shaping and bending of the neural plate. J. Comp. Neurol. *381*, 473–488.

Schoenwolf, G.C., and Smith, J.L. (1990). Mechanisms of neurulation: traditional viewpoint and recent advances. Development *109*, 243–270.

Sherrard, K., Robin, F., Lemaire, P., and Munro, E. (2010). Sequential activation of apical and basolateral contractility drives ascidian endoderm invagination. Curr. Biol. *20*, 1499–1510.

Straight, A.F., Cheung, A., Limouze, J., Chen, I., Westwood, N.J., Sellers, J.R., and Mitchison, T.J. (2003). Dissecting temporal and spatial control of cytokinesis with a myosin II Inhibitor. Science *299*, 1743–1747.

Vielemeyer, O., Nizak, C., Jimenez, A.J., Echard, A., Goud, B., Camonis, J., Rain, J.-C., and Perez, F. (2010). Characterization of single chain antibody targets through yeast two hybrid. BMC Biotechnol. *10*, 59.

Wallingford, J.B., and Harland, R.M. (2002). Neural tube closure requires Dishevelled-dependent convergent extension of the midline. Development *129*, 5815–5825.

Wallingford, J.B., Fraser, S.E., and Harland, R.M. (2002). Convergent extension: the molecular control of polarized cell movement during embryonic development. Dev. Cell *2*, 695–706.

Wallingford, J.B., Niswander, L.A., Shaw, G.M., and Finnell, R.H. (2013). The continuing challenge of understanding, preventing, and treating neural tube defects. Science *339*, 1222002.

Winter, C.G., Wang, B., Ballew, A., Royou, A., Karess, R., Axelrod, J.D., and Luo, L. (2001). Drosophila Rho-associated kinase (Drok) links Frizzled-mediated planar cell polarity signaling to the actin cytoskeleton. Cell *105*, 81–91.

Yamaguchi, Y., and Miura, M. (2013). How to form and close the brain: insight into the mechanism of cranial neural tube closure in mammals. Cell. Mol. Life Sci. *70*, 3171–3186.

Yamaguchi, Y., Shinotsuka, N., Nonomura, K., Takemoto, K., Kuida, K., Yosida, H., and Miura, M. (2011). Live imaging of apoptosis in a novel transgenic mouse highlights its role in neural tube closure. J. Cell Biol. *195*, 1047–1060.

Zeller, R.W., Virata, M.J., and Cone, A.C. (2006). Predictable mosaic transgene expression in ascidian embryos produced with a simple electroporation device. Dev. Dyn. *235*, 1921–1932.

Developmental Cell

Supplemental Information

Sequential Contraction and Exchange of Apical Junctions Drives Zippering and Neural Tube Closure in a Simple Chordate

Hidehiko Hashimoto, Francois B. Robin, Kristin M. Sherrard, and Edwin M. Munro

Supplemental Figure 1

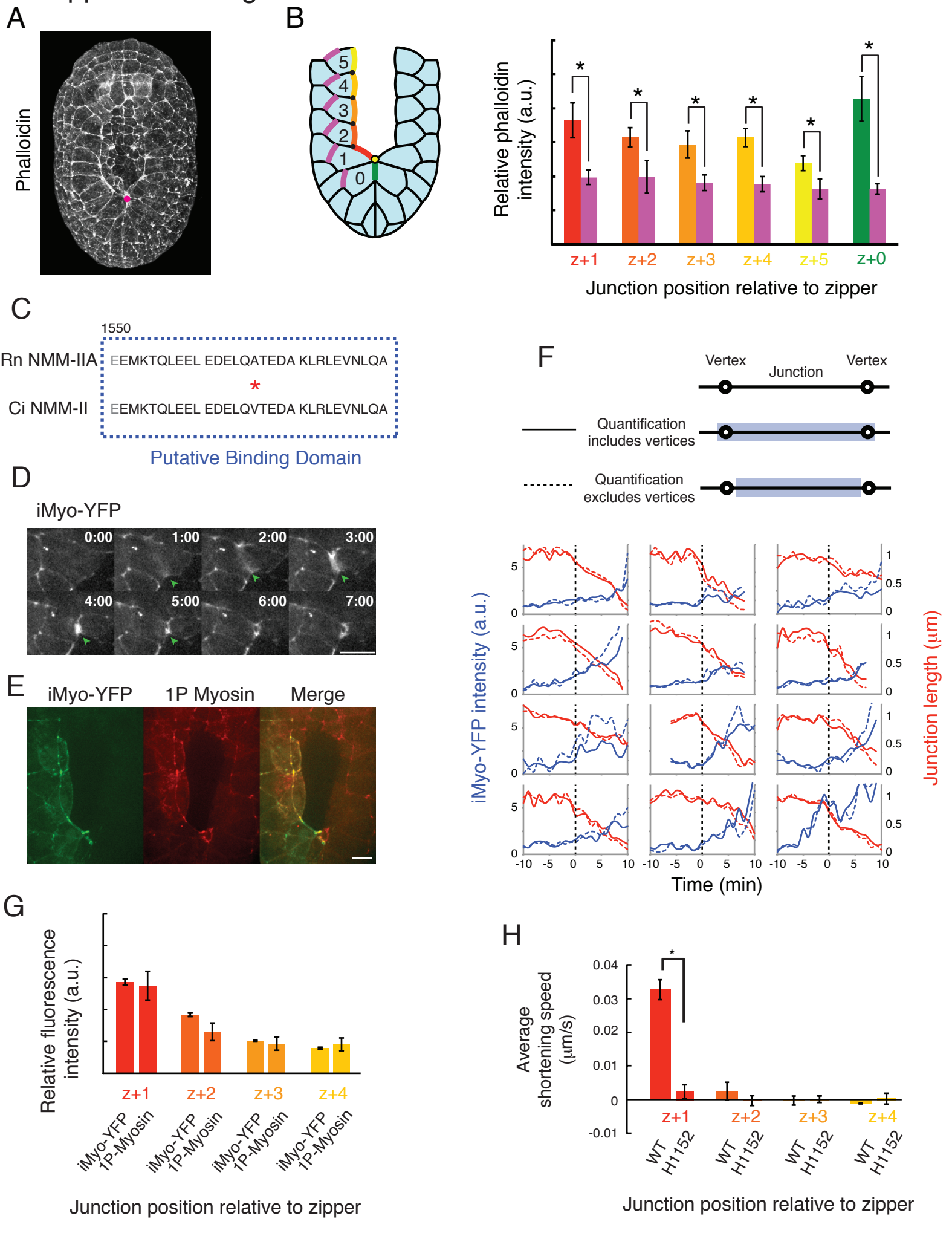

Figure S1. **Junction contraction and zipper progression require ROCK-dependent myosin contractility (related to Figure 4).** (A) 3D surface rendering in dorsal view of an embryo fixed and stained with phalloidin. Magenta dot indicates zipper position. (B) Average relative phalloidin intensity measured along junctions of the types indicated in the schematic to the left, which are color-coded as follows: Sequence of red-yellow represents proximal-distal Ne/Epi junction position *relative* to the zipper; purple is the corresponding Epi/Epi control junction; green indicates new Epi/Epi junction behind the zipper. Fixation, staining and measurements are performed at the stage shown in (A). *: $P < 0.05$, Student's *t* test. Error bars are SEM (n=10). (C) Sequence alignment between the putative intrabody binding domain of rat non-muscle Myosin IIA (Rn NMM-IIA) and the corresponding sequence in *Ciona* non-muscle myosin II (Ci NMM-II). (D) iMyo-YFP accumulates at the cleavage furrow during cell division (green arrowheads). (E) iMyo-YFP colocalizes with active (1P) Myosin. Maximum intensity projection of embryos electroporated with pFOG::iMyo-YFP and stained with anti-1P-myosin antibody. Green channel: iMyo-YFP. Red channel: 1P-Myosin antibody. The restricted expression domain of iMyo-YFP is due to mosaic expression downstream of the tissue-specific FOG promoter. (F) Quantification of junctional iMyo-YFP intensity is insensitive to inclusion/exclusion of vertices. Top schematic indicates measurements of juntional iMyo-YFP intensity +/- vertices. Graphs show the distribution of iMyo-YFP during individual junction shortening events. Red line: Normalized junction length. Blue line: relative iMyo fluorescence intensity averaged along the junction. Dashed lines: quantification excluding the vertices. Plain lines: quantification including the vertices. Vertical black dashed line indicates the time at which the junction shortens past 90% of plateau junction length preceding the shortening. (G) Comparison of relative junctional intensity of iMyo-YFP and 1P Myosin with respect to junction position (junction positions relative to zipper are color-coded as in (B)). Myosin relative intensity at Ne/Epi junction ahead of the zipper in iMyo-YFP electroporated embryos (live) or stained with anti-1P-myosin antibody (fixed). (H) Comparison of average shortening speed of Ne/Epi junctions ahead of the zipper in control and H1152-treated embryos (n>12 cells from 4 embryos for each condition).

Supplemental Figure 2

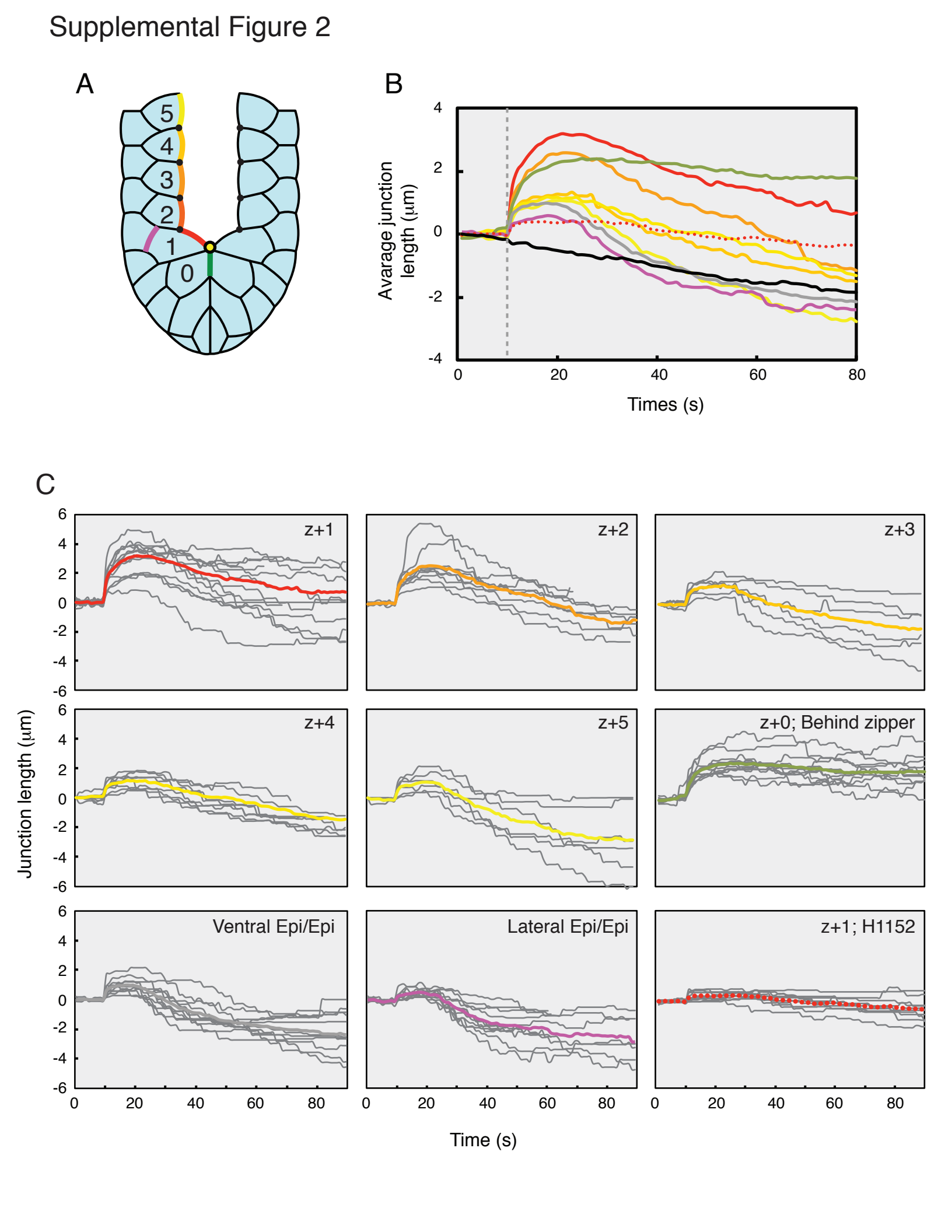

Figure S2. **Detailed analysis of junction tension by laser ablation (related to Figure 5).** (A) Schematic view of the dorsal surface with distinct junction types color-coded. Sequence of red-yellow represents proximal-distal Ne/Epi junction position *relative* to the zipper; purple is the corresponding Epi/Epi control junction; green indicates new Epi/Epi junction behind the zipper. (B) Time course of changes in junction length following laser ablation for the different junction types indicated in (A). Dashed vertical gray line indicates the time of ablation, t = 10s. Each trace shows the difference between the junction length and its average length during the 10s preceding the ablation, averaged over many individual ablation experiments (see Figure 5). Black line corresponds to the junction ahead of the zipper in the absence of laser ablation. (C) Original data yielding the averaged traces displayed in (B). As in Figure 5, red dashed line corresponds to H1152-treated embryos.

Supplemental Figure 3

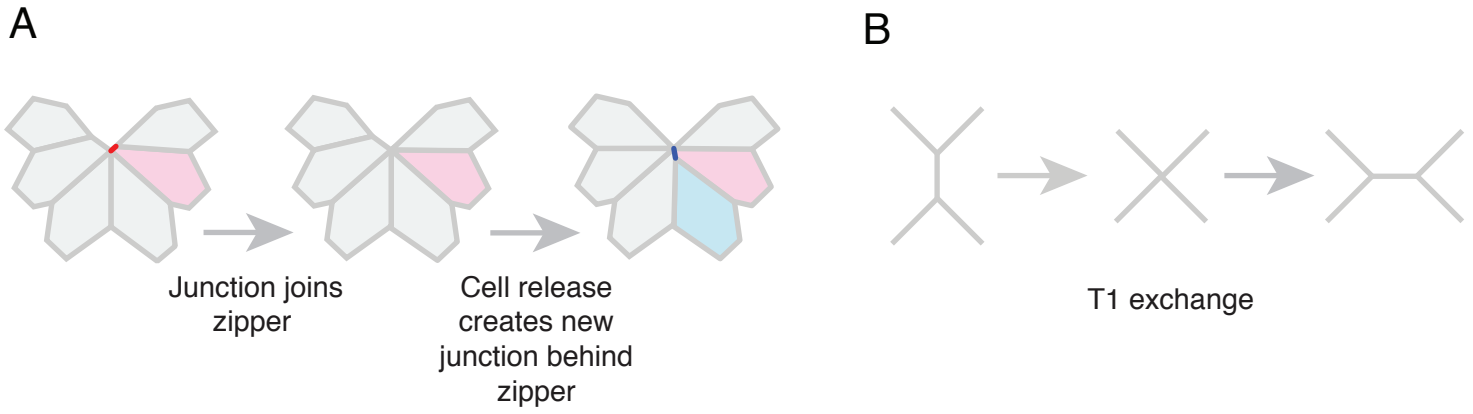

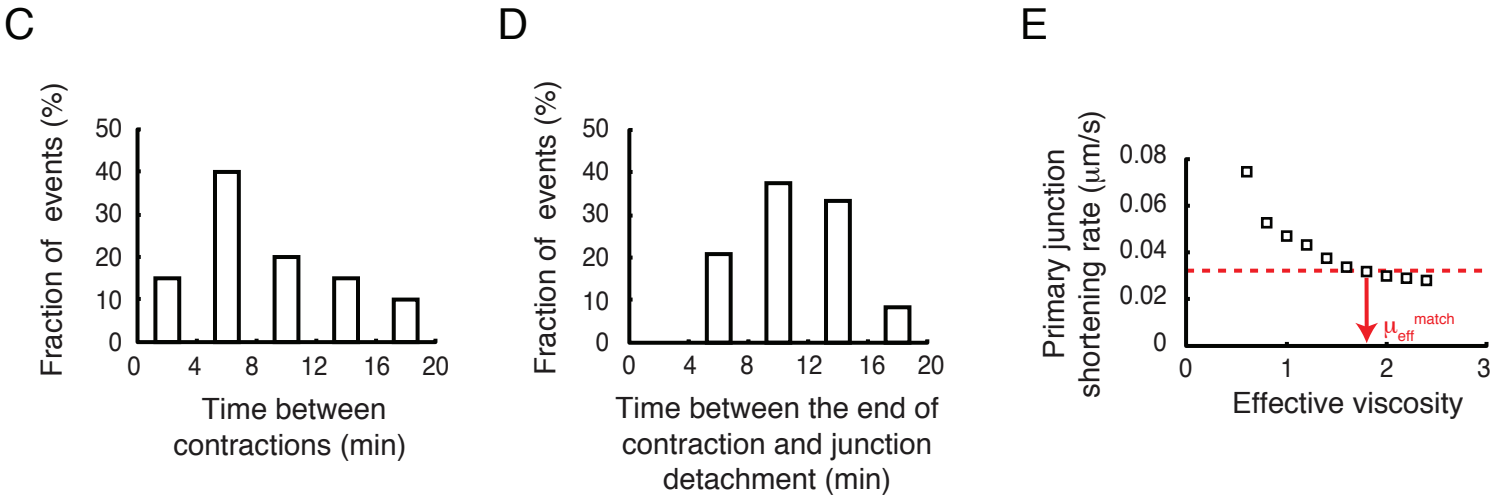

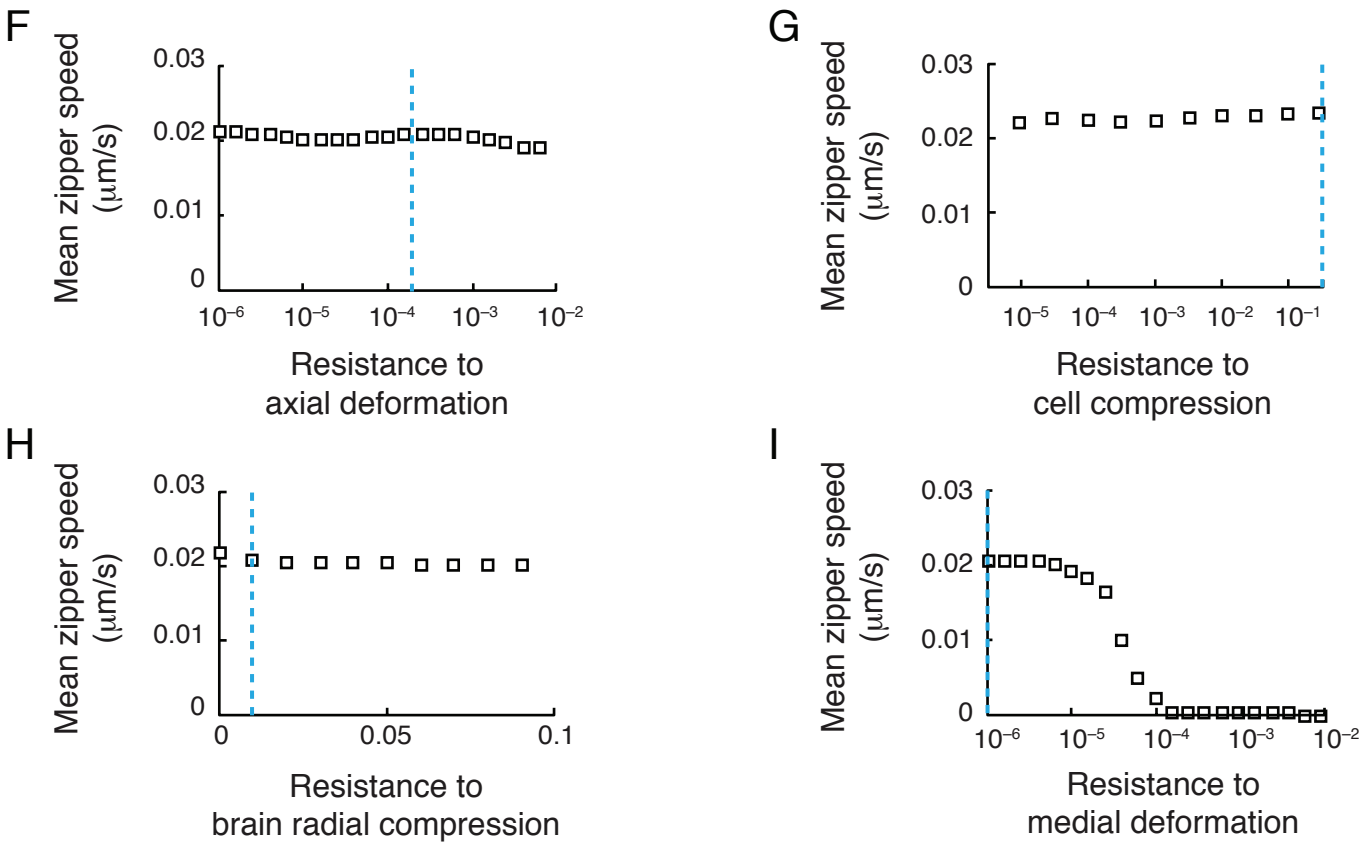

Figure S3. **Experimental determination of simulation parameters, and insensitivity of zippering speed to parameter variations for different modeling assumptions (related to Figure 6).** (A) Schematic view of model assumptions concerning junction merger and cell detachment from the zipper. Left panel: A junction merges with the zipper when its length falls below a threshold value (0.25 μm). Middle: junction exchange occurs. Right: junction exchange is complete; the cell detaches and a new junction is created behind the zipper. (B) Simpler T1 transitions are also allowed to occur when internal junctions shrink below 0.5μm in length. (C) Experimentally measured distribution of time lags between successive contractions of the primary junction, yielding an average of ~504 s ± 324 s (standard deviation). (D) *In vivo* measurements of delay between end of contraction and cell detachment, corresponding to the resolution of the junction exchange, yielding an average of ~588 s ± 201 s (standard deviation). (E) Determination of a value for effective viscosity. Average rate of primary junction contraction *in silico* for a range of values of the effective viscosity μ_{eff}. Dashed red line indicates the experimentally measured average contraction speed of 0.032 μm/s. The best match is obtained for μ_{eff} ~1.8. (F-I) Dependence of zipper speed on the values of parameters governing: (F) resistance to axial displacement of cells along the Ne/Epi boundary (representing attachment to the underlying neural tube and notochord), (G) resistance to changes in cell area, (H) radial forces on anterior Ne/Epi junctions, representing the resistance of the brain to compression, and (I) resistance to medial displacement of cells at the Ne/Epi boundary, representing resistance to medial bending of the underlying neural primordium.

Supplemental Figure 4

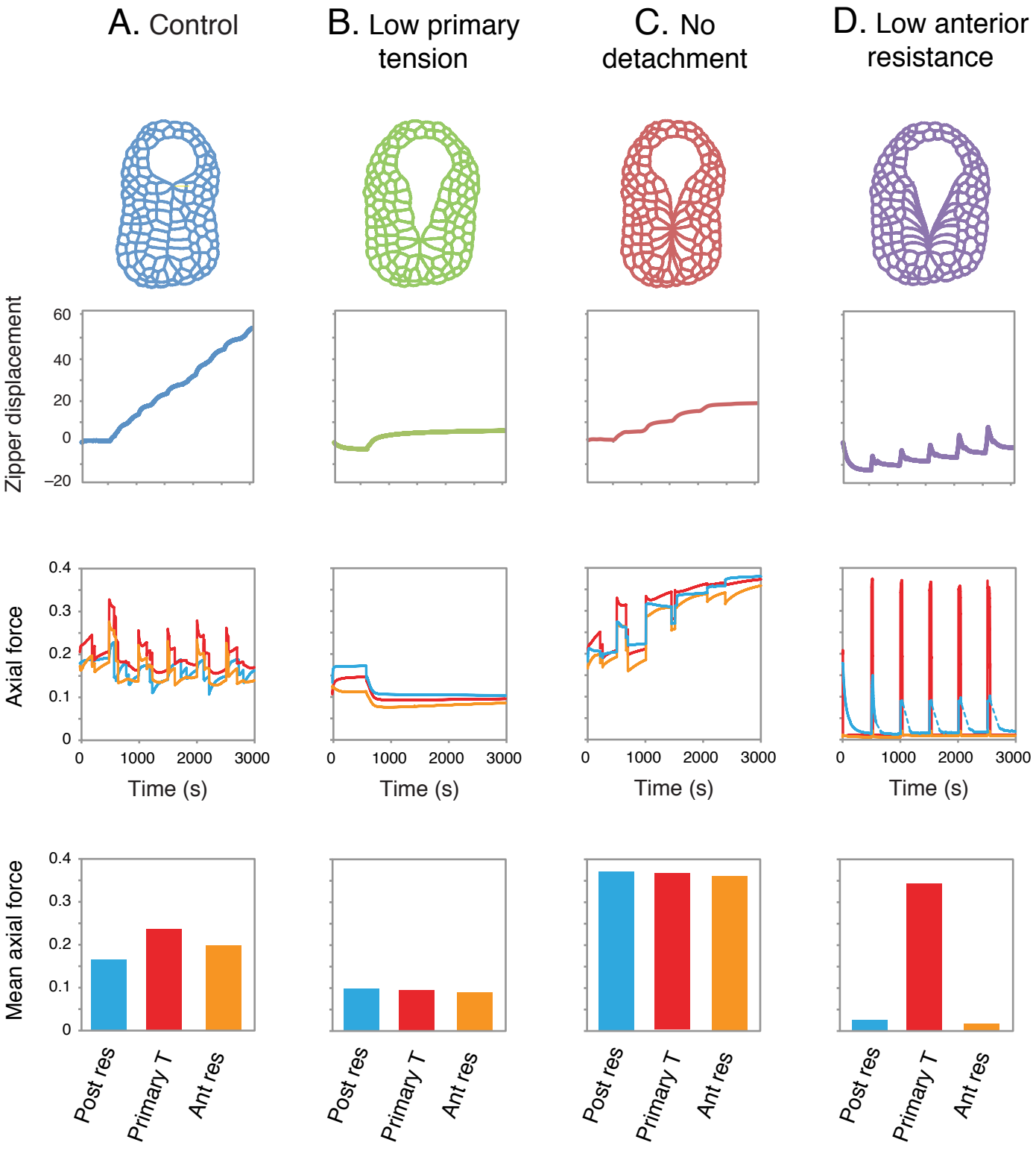

Figure S4. **Dependence of zippering on the force balance across primary junctions (related to Figure 6).** The top row shows simulation snapshots and plots of zipper displacement *vs* time for different manipulations of the junctional force balance, taken from Figure 6D&E. The second row shows plots of primary contraction force, anterior tissue resistance and posterior tissue resistance vs time. The third row shows the relative magnitudes of primary contraction force, anterior tissue resistance and posterior tissue resistance taken at T = 3000s (B&C) or averaged from T = 0 to 3000s (A&D). **(**A) Control simulations using reference values for all parameters; (B) Reducing the primary junction tension to 0.1 causes the zipper to stall with equally low levels of anterior and posterior tissue resistance. (C) Disallowing cell detachment causes the zipper to stall with a buildup of both anterior and posterior tissue resistance to equally high levels as primary contractions and zipper advance recruit and realigned junctions ahead of and behind the zipper (see Figure 6D). (D) Reducing tension on all Ne/Epi junctions anterior to the zipper and all Epi/Epi junctions that radiate from the Ne/Epi boundary ahead of the zipper to 0.005 causes a strong reduction in zippering speed with equally low levels of anterior and posterior tissue resistance. Note that zippering does not stall completely, because viscous resistance to stretching of anterior junctions can support transient zipper advance during rapid primary contractions.

Movie Legends

Movie S1 (related to Figure 1): Overview of entire neural tube closure. Anterior is top. Embryo was stained with FM4-64. Each frame is the maximum intensity projection of 20 focal planes spaced at 1 μm in Z and acquired at 60s intervals. The movie is displayed at 30 frames per second (fps).

Movie S2 (related to Figure 2): Comparison of zippering and neural tube closure in anterior and posterior half embryos. Sibling control embryo (left), anterior half embryo (middle) and posterior half embryo (right) were stained with FM4-64 and imaged under identical conditions simultaneously. Each frame is the maximum intensity projection of 21 focal planes spaced at 0.75 μm in Z and acquired at 60s intervals. The movie is displayed at 30 fps.

Movie S3 (related to Figure 3): Time lapse movie of junctional dynamics during zippering in an embryo expressing ZO1-GFP under the control of a promoter that drives expression in all epidermal cells and a subset of neurectoderm cells lying along the Ne/Epi boundary. Because of mosaic transgene expression, only half the embryo expresses ZO1-GFP. Each frame is the maximum intensity projection of 11 images collected at 0.75 μm intervals in Z near the apical surface; frames were collected at 10s intervals. The movie is displayed at 30 fps.

Movie S4 (related to Figure 4): Myosin II dynamics during zippering in live embryos expressing iMyo-YFP. Because of mosaic transgene expression, only half the embryo expresses iMyo-YFP. Each frame is the maximum intensity projection of 15 images collected at 0.75 μm intervals in Z near the apical surface; frames were collected at 60s intervals. The movie is displayed at 25 fps.

Movie S5 (related to Figure 4): Blebbistatin treatment inhibits neural invagination, Ne/Epi junction contraction and zippering. Control embryo (Left) and embryo (Right) exposed to 100μM blebbistatin from 300 s after starting imaging. Embryos were stained

with FM-464 and imaged as described in Materials and Methods. Each frame is the maximum intensity projection of 21 focal planes spaced at 1 μm in Z and acquired at 120s intervals. The movie is displayed at 15 fps.

Movie S6 (related to Figure 4): Treatment with Rho kinase inhibitor H1152 inhibits Ne/Epi junction contraction and zippering. (Left) Control embryo. (Right) Embryo exposed to 1μM H1152 from 600s before we began imaging. Embryos were stained with FM-464 and imaged as described in Materials and Methods. Each frame is the maximum intensity projection of 21 focal planes spaced at 1 μm in Z and acquired at 60s intervals. The movie is displayed at 15 fps.

Movie S7 (related to Figure 4): Time-lapse movies of neurula-stage embryos expressing a dominant-negative form of RhoA. (Left) RhoA DN and GFP were expressed broadly in the right posterior epidermal cells ***but not in*** the single rows of Ne and Epi cells flanking the Ne/Epi boundary. (Right) RhoA DN and GFP were expressed only in the right posterior single rows of Ne and Epi cells flanking the Ne/Epi boundary. Embryos were stained with FM-464 and imaged as described in Materials and Methods. GFP, labeling cells expressing RhoA DN, is green. FM-464, labeling all cell membranes, is white. Each frame is the maximum intensity projection of 15 images collected at 0.75 μm intervals in Z near the apical surface; frames were collected at 60s intervals. The movie is displayed at 25 fps.

Movie S8 (related to Figure 5): Examples of junction response to laser ablation in embryos expressing ZO1-GFP. (Left) Response of a Ne/Epi junction just ahead of the zipper (position z+1 in the schematic view of Fig. 5A). (Right) Response of an Ne/Epi junction far ahead of the zipper (position z+4 in the schematic view of Fig. 5A). Each frame is the maximum intensity projection of 3 images collected with a Z-step of 1.5 μm near the apical surface; frames were collected at 1s intervals. The movie is displayed at 30 fps.

Movie S9 (related to Figure 6): Comparison of *in vivo* and *in silico* zippering. (Left)

Control embryo stained with FM4-64 and imaged as described above. (Right) Simulated zippering, using experimentally measured/constrained reference values for relative junction tensions, intervals between primary contractions, delay between the end of primary contraction and cell detachment and effective viscosity. See main text and Supplementary Methods for parameter values and details. Time compression is 60s/frame for both the real and simulated data and the movie is displayed at 30 fps.

Movie S10 (related to Figure 6): Comparison of *in silico* zippering for the following conditions. (Left) "Control" embryos using experimentally measured/constrained reference values for relative junction tensions, intervals between primary contractions, delay between the end of primary contraction and cell detachment and effective viscosity. See main text and Supplementary Methods for parameter values and details. (Second from left): Reduced primary contraction. Tension on the primary junction was set to 0.1. (Third from left) No cell detachment behind zipper. (Fourth from left) Tension on all Ne/Epi junctions anterior to the zipper and all Epi/Epi junctions that radiate from the Ne/Epi boundary ahead of the zipper were reduced to 0.005. (Right) Simulation of a posterior half embryo. Time compression is 60s/frame for both the real and simulated data and the movie is displayed at 30 fps. Analysis of force balance for these conditions (excluding the posterior half embryo) is shown in Figure S4.

Movie S11 (related to Figure 8): Comparison of (left) sequential and (right) uniform modes of Ne/Epi boundary contraction. Initial conditions are the same for both simulations. In the uniform contraction case, all Ne/Epi junctions contract continuously with the same strength as the primary junction in the sequential case. In both cases, Ne/Epi junctions at the boundary between epidermis and anterior brain contract with a lower tension. All other parameters were set to reference values for both cases. Time compression is 60s/frame and the movie is displayed at 30 fps.

Movie S12 (related to Figure 8): Comparison of zippering in idealized small (Left) and large (Right) embryos. Simulation on the left shows an idealized epidermis with identical rules, parameter values and roughly the same number of cells as in the ascidian-specific

simulations. Simulation on the right represents a photographic enlargement of the first by a factor of 5, but with the same cell size and simulation parameters. We used an idealized geometry to facilitate direct comparison. In both simulations, cell boundaries at the top and bottom are constrained such that they can move/deform in the horizontal, but not in the vertical direction. For the embryo at the left, frames are taken at 20-second intervals, for the embryo on the right, frames were taken at 100 second intervals.

Supplemental Experimental Procedures

Embryo culture

Fertilization, staging, dechorionation and electroporation were conducted as previously described (Corbo et al., 1997; Bertrand et al., 2003, Hotta et al., 2007). We cultured embryos in 5-cm plastic petri dishes coated with 1% agarose and filled with HEPES-buffered artificial seawater (ASWH) (Pasini et al, 2006).

Embryo microsurgery

We performed cutting experiments just before the initiation of zippering at Stage 15 (Hotta et al., 2007). We cut embryos under a Nikon SMZ645 stereomicroscope using hand-held glass needles pulled from 100µl glass capillaries. We then cultured anterior and posterior embryo halves in ASWH and then imaged or processed them for fixation under the same conditions as uncut controls.

Treatment with H1152 and Blebbistatin

We treated embryos with 1 µM H1152 (Enzo Life Sciences) and 100 µM Blebbistatin (Sigma, B0560-1MG) dissolved in ASWH. We exposed embryos continuously starting just before the onset of zippering Stage 15 (Hotta et al., 2007) and then we imaged or cultured them prior to fixation and staining under the same conditions as control embryos.

Immunostaining and quantitative analysis of F-actin and phosphomyosin distributions

We fixed and stained embryos with alexa 488 phalloidin (Invitrogen) and a mouse polyclonal antibody raised against ser19-phosphorylated myosin regulatory light chain (1P myosin, Cell Signaling) as previously described (Sherrard et al, 2010) with one exception: for immunostaining of 1P myosin, we blocked embryos with 1% BSA in PBT for 24 hour at 4 ℃ before incubating them in the primary antiserum. We collected Z-stacks of confocal images on a Zeiss LSM 510 confocal microscope with 40×/1.3 oil-immersion objective at 0.5 to 1 μm intervals. We rendered 3D projections in ImageJ 3D

Viewer (http://rsbweb.nih.gov/ij/plugins/3d-viewer/). We measured relative levels of junctional F-actin and 1P myosin by measuring fluorescence intensities from maximum intensity projections of the apical surface. Specifically, we measured the intensities along cell junctions in ImageJ (http://rsbweb.nih.gov/ij/) as mean gray levels averaged over 10 pixels thick lines drawn along the junction of interest.

Fusion constructs

We amplified 3xGFP from an Ensconsin-3xGFP entry clone (Roure et al, 2007), digested with *BglII* and *EcoRV*, and inserted into the 3' entry site of a standard Gateway RfA cassette in pFOG::RfA (Roure et al, 2007). We then recombined a Gateway entry clone containing the full sequence coding Ciona ZO1 (Ci-ZO1) (Sherrard et al, 2010) using the Gateway LR reaction (Invitrogen) into the pFOG::RfA-3xGFP destination vector yielding pFOG::ZO1-3xGFP (hereafter ZO1-GFP).

We amplified by PCR the coding sequence of the myosin intrabody from a plasmid kindly provided by Frank Perez (SF9-YFP), and cloned it into pCR8-gw-TOPO using TOPO TA cloning (Invitrogen). We subsequently recombined the intrabody entry clone into pFOG::RfA using the Gateway LR reaction (Invitrogen), yielding pFOG::iMyo-YFP (hereon iMyo-YFP).

We recombined entry clones containing a dominant negative form of *Ciona intestinalis* RhoA (Philips et al, 2003; hereafter RhoA DN) and GFP into the pFT::RfA (pFT: promoter Fucosyl-Transferase, Pasini et al, 2012) using the Gateway LR reaction (Invitrogen), yielding pFT::RhoA DN and pFT::GFP respectively.

4D **time-lapse imaging**

For live time-lapse imaging, we settled embryos onto gelatin-formaldehyde coated (Robin et al, 2011) glass bottom plates (TED PELLA) filled with seawater and maintained at 15 – 18˚C. We labeled apical junctions by electroporating newly fertilized zygotes with ~70µg ZO1-GFP, and we labeled cell membranes using the fluorescent lipophilic dye FM4-64 (5µg/ml, Molecular Probes, #T13320). Laser illumination at 488nm for GFP (resp. 561nm for FM4-64) from a 50mW solid state Sapphire laser (Coherent) was delivered by fiber optics to a Yokogawa CSU-X1 spinning disk scan head

installed on a Nikon ECLIPSE-Ti inverted microscope, yielding an effective power of 9.1 mW (resp. 14.1 mW). We routinely used 20% of the laser power for imaging on both channels. We collected whole embryo views (resp. magnified views of the zipper region) using 20×/0.75NA (resp. 60×/1.2NA) water-immersion objectives, magnified by ~ 2.25x (resp. 1.5x) onto a Rolera em-c^2 EM-CCD. We acquired confocal stacks using an x-y motorized stage (for multiple-location imaging) and a fast piezoelectric Z-axis stepper motor with focus steps taken at 0.5 to 1 μm intervals. We performed all image analysis and processing in ImageJ using publicly available plugins (LOCI, StackReg).

Measurements of iMyo-YFP intensity vs junction length.

We measured relative iMyo YFP intensities along individual junctions in ImageJ as mean gray levels averaged over 10 pixels thick line drawn along the junction of interest. In one case, we measured the average intensity along the entire junction including the endpoints where iMyo-YFP is most highly concentrated. In a second set of measurements, we excluded the endpoints. We show the measurement excluding endpoints in Figure 4C, but the results were very similar for both measurements (see Figure S1G).

We aligned data from multiple junctions (Figure 4D) with respect to the onset of contraction, which we measured as follows: Working back from the end of the contraction we identified the first 10-frame window in which the average shortening rate fell below 0.5μm/min. We measured a pre-contraction plateau length as the average length in the 10 frames immediately preceding this window; then we took the onset of contraction to be the first frame at which the junction length fell below this plateau length. For the analysis shown in Figure 4C&D, we focused on the subset of junctions for which a clear pre-contraction plateau could be discerned.

Supplementary modeling procedures

Overview. The modeling approach that we used was previously described by Sherrard et al (2010). For clarity, we include elements of that description here. We assume that the essential mechanics which govern zippering operate at/near the apical surface of the neuroectoderm, consistent with our observation that actomyosin is enriched specifically at the subapical margin and by the fact that we infer relative tensions from laser ablations performed on cell-cell junctions at or near the apical surface. Accordingly, we represent the dorsal surface of a neurula stage ascidian embryo as a sheet of 2D cells (see Figure 6A). We represent each epidermal cell explicitly, while the mechanical contributions of axial neural tube and the presumptive brain appear implicitly as forces imposed on individual epidermal cells (see below).

We model each cell in two dimensions as a collection of discrete elements, joined together to form a continuous boundary with surface area *A*. Adjacent cells share elements along common boundaries, which we call junctions. Along each junction, elements are connected directly to one another at nodes, which serve as material points of reference. At points where 3 junctions meet, elements are connected to a single common vertex by simple linear springs (Figure A1).

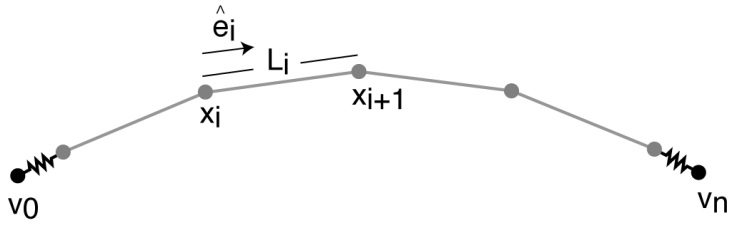

Figure A1. Model representation of a single cell boundary as a collection of interconnected elements.

Mechanical properties of cortical elements. We endow each junction element with a active tension T, whose magnitude reflects the strength of actomyosin contractility, and an effective viscosity μ_{eff}, which represents the tendency of the cell cortex to creep or flow in response to externally applied forces, or gradients in active tension, on the timescale (minutes) over which cell shape changes occur (Bray and White, 1988, Bausch et al, 1999, Mayer et al, 2010). We assume that the value of T is the same for all elements within a given junction, but can change over time for each junction by rules given below. For simplicity, we assume that μ_{eff} is the same for all junction elements, regardless of boundary type.

With these assumptions, the force that a junction element i exerts upon its neighbors at nodes i and i+1 is +/- $\vec{F}^{i}_{cortex}$ respectively, where

(1) $$\vec{F}^{i}_{cortex} = \left[T + \frac{\mu_{eff}}{L_i} \frac{dL_i}{dt} \right] \hat{e}_i$$

where L_i is the instantaneous length of element i, and $\hat{e}_i$ is a unit vector lying tangent to boundary element i and pointing towards node i+1 (Figure A1).

The second term in brackets is a "viscous tension" that arises from an effectively viscous resistance to changes in the segment length L_i, which is equal to the effective viscosity μ_{eff} times the strain rate $\frac{1}{L_i}\frac{dL_i}{dt}$. The contribution of this term can be best appreciated by

considering an isolated segment subjected to an active (e.g. actomyosin-based) force T. The segment will tend to shorten ($\frac{dL_i}{dt} < 0$) leading to $\frac{\mu_{eff}}{L_i}\frac{dL_i}{dt} < 0$. Thus the term in brackets in (1) is less than T. In other words, when an active tension given by T causes a segment to shorten, it works against an effective resistance, given by $\frac{\mu_{eff}}{L_i}\frac{dL_i}{dt} < 0$, and this reduces the net force produced by that segment - $\vec{F}^i_{cortex}$ - to less than T.

We write the segment length as $L_i = [(x_{i+1} - x_i)^2 + (y_{i+1} - y_i)^2]^{1/2}$ where $\vec{x}_i = (x_i, y_i)$ are the coordinates of the i^{th} node, and then apply the chain rule and rearrange terms to obtain:

(2) $$\frac{1}{L_i}\frac{dL_i}{dt} = \frac{1}{L_i^2}\left[(x_{i+1} - x_i) * (\frac{dx_{i+1}}{dt} - \frac{dx_i}{dt}) + (y_{i+1} - y_i) * (\frac{dy_{i+1}}{dt} - \frac{dy_i}{dt})\right]$$

Substituting into Equation 1, we obtain:

(3) $$\vec{F}^i_{cortex} = \left[T + \frac{\mu_{eff}}{L_i^2}\left[(x_{i+1} - x_i) * (\frac{dx_{i+1}}{dt} - \frac{dx_i}{dt}) + (y_{i+1} - y_i) * (\frac{dy_{i+1}}{dt} - \frac{dy_i}{dt})\right]\right]\hat{e}_i$$

Vertex Spring Forces. We connect the terminal cortical nodes of each junction to a common vertex through simple linear springs:

(4) $$\vec{F}^i_{vertex} = k_s(\vec{v} - \vec{x}_i),$$

where k_s is the spring stiffness, $\vec{v}$ is the vertex position, and $\vec{x}_i$ is the position of a terminal cortical node.

Resistance to surface area change. During zippering in vivo, epidermal cells undergo variation in apical surface area due to changes in junctional tension, external forces from surrounding cells/tissues, and possibly changes in cellular volume. These changes are relatively minor (< 20% on average for cells along the Ne/Epi boundary). For simplicity, therefore, we assume that the apical surface area A of each epidermal cell remains roughly constant, and we enforce this by imposing a pseudo-pressure force normal to each junction element:

(5) $$\vec{F}_{pressure} = \beta * L_i * \frac{A - A_0}{A_0} \hat{n}_i \ ,$$

where A is current cell area, A_0 is the initial area, L_i is segment length, $\hat{n}_i$ is the unit outward normal to that segment, and β is a constant. This is analogous to the area elasticity term used in simple vertex models (e.g. Farhadifar et al, 2007).

For most of the simulations reported here, we set β to the minimal value required to maintain cell surface areas within 95% of the target. However, reducing β over 4 orders of magnitude (leaving all other parameters constant) has almost no effect on the predicted zippering speed, although it does affect the details of how individual cells change shape and apical surface area during zippering. Thus the main conclusions of our study are

unlikely to depend on the exact nature or magnitude of this constraint.

Modeling mechanical contributions of the axial nerve cord and presumptive brain.

During zippering, the epidermis is constrained by its attachment to the underlying neural tube, which itself is strongly attached to the notochord (Munro and Odell, 2002). In initial simulations, we found that the model embryo shortens slightly during zippering, which is presumably resisted in real embryos by attachment to the underlying tissues. To explore how this might bias our simulation results, we modeled a simple form of elastic resistance in which each cell lying along the Ne/Epi boundary experiences a net axial force proportional to its axial length L_{axial} and to the distance between the current axial position of the cell centroid $C_x(t)$ and its initial position $C_x(0)$:

(6) $$F_{axial} = k_{axial} L_{axial} (C_X(t) - C_X(0))$$

This force is distributed to the individual segments that comprise the cell boundary in proportion to their lengths. Thus:

(7) $$F^i_{axial} = k_{axial} L_{axial} (C_X(t) - C_X(0))$$

This is clearly a very crude representation of the real tissue mechanics. Our goal was not to capture a realistic model of the 3D mechanics, but rather to assess the extent to which the zippering mechanism we describe here is sensitive to the global mechanical context.

In fact, we find that simulated zippering speed is highly insensitive to the exact nature and magnitude of the axial resistance (Figure S3F and data not shown).

We modeled a resistance to bending motions of the neural tube perpendicular to the AP axis as a force on epidermal cells along the Ne/Epi boundary proportional to L_{axial} and the medial strain, which we define to be the difference between the current and initial positions of the cell centroid perpendicular to the AP axis divided by the initial position:

(8) $$F_{prop} = k_{prop} L_{axial} \frac{C_Y(t) - C_Y(0)}{C_Y(0)}$$

with a force on individual boundary elements given by:

(9) $$F^i_{prop} = k_{prop} L_{axial} \frac{C_Y(t) - C_Y(0)}{C_Y(0)}$$

Finally, we modeled the presumptive brain as a single large cell with constant area constraint, enforced as described above, such that the force on each of the junction elements bordering the brain is given by:

(10) $$\vec{F}^i_{brain} = \beta_{brain} * L_i * \frac{A_{brain} - A^0_{brain}}{A^0_{brain}} \hat{n}_i$$

where A_{brain} is current area of the "brain cell", A^0_{brain} is its initial area, L_i is the element length, $\hat{n}_i$ is the unit outward normal to that element, and β_{brain} is a constant.

Putting (6)-(10) together, the net force on a boundary element i due to external constraints is:

$$\vec{F}^i_{ext} = \vec{F}^i_{axial} + \vec{F}^i_{prop} + \vec{F}^i_{brain} \tag{11}$$

where it is understood that the individual terms represent the summed contributions from any relevant cells to which that element is attached.

Equations of motion. Collecting (3), (4), (5) and (11) together, applying Newton's second law, and neglecting inertial forces, which are small at cellular length scales, we have for the i^{th} junction node:

$$\vec{F}^i_{cortex} - \vec{F}^{i-1}_{cortex} + \vec{F}^i_{vertex} + \vec{F}^i_{pressure} + \frac{\vec{F}^i_{ext} + \vec{F}^{i-1}_{ext}}{2} - \mu_g \frac{\vec{x}_i}{dt} = 0, \tag{12}$$

$$i = 0, \ldots, n$$

Enumerating equation (12) over all nodes i yields an implicitly coupled system of ordinary differential equations that we solve numerically using standard methods (see Sherrard et al, 2010) to predict the system dynamics.

The last term in (12) could be interpreted as a "frictional" resistance to motion of the cell boundary relative to a fixed coordinate system. However, it is not intended to represent a specific physical effect. Without this term, the equations of motion are not well-posed because they are indifferent to rigid body translations of the boundary. That is, the same equations would yield an infinity of different solutions in which the simulated tissue deforms in exactly the same way, but translates through space in different directions and at different speeds. Choosing a non-zero value for the "friction" parameter μ_g ensures that we get a unique solution.

In practice, we set the value of μ_g small enough that it contributes negligibly to the simulated dynamics to ensure that we are not introducing an unanticipated physical effect.

This friction term *could be* interpreted as arising from resistance to the motion of cells relative to the surrounding sea water. However, that resistance is almost certainly negligible relative to the internal resistances represented by effective viscosity in our simulations. A simple justification for this assertion is that one can push an ascidian embryo rapidly through sea water with a thin glass needle without indenting its surface or causing any visible shape change.

In principle, the friction term could also represent a resistance to sliding of epidermal cells relative to neighboring tissues (e.g. the underlying neural tube. While it might be interesting to explore such effects in future work, we could see no experimental basis for considering them in the present study.

Assigning model parameter values

Rules for assigning junction tensions.

We assigned values for junction tensions based on our laser ablation results (Figure 5C), distinguishing the following values: Primary Ne/Epi (one from zipper), secondary Ne/Epi (two from zipper), all other Ne/Epi, new-formed Epi/Epi, and all others (Figure 6A). These values are determined by our laser ablation results up to a scale factor, which represents an arbitrary choice of units of force. Thus only the relative values of force are significant.

Based on our experimental observations, we imposed a strict posterior to anterior sequence of all-or-none primary contractions along the Ne/Epi boundary. We set the interval between the initiation of primary contractions $t_{contract}$ to the average value measured in embryos (504 sec; see Figure S3D) and the first junctions initiated strong primary contraction at simulation time $t = 0$. Once a junction initiates primary contraction, it continues to do so until it joins the zipper (see below). Given this fixed schedule of primary contractions, we assigned tensions to junctions along the Ne/Epi boundary as follows:

(i) A junction undergoing primary contraction has tension T_1, regardless of its position relative to the zipper.

(ii) Junctions adjacent to the zipper that are not undergoing primary contraction contract with tension T_2

(iii) Junctions one away from the zipper that are not undergoing primary contraction contract with tension T_2 if the neighboring junction that is adjacent to the zipper is undergoing primary contraction, else they contract with tension T_3

(iv) All other junctions along the Ne/Epi boundary contract with tension T_3

(v) Junctions that form when cells release from the zipper contract with tension T_{behind}.

(vi) All other junctions contract with tension T_{epi}

The relative values for T_1, T_2, T_3, T_{behind} and T_{epi} were taken directly from the laser ablation measurements reported in Figure 5.

Rules for junction exchange and release.

We allowed two types of junction exchange. When the length of an Ne/Epi junction adjacent to the zipper falls below a minimum value L_{min}, it is immediately merged with the zipper vertex (Figure S3A). The cell containing that junction then remains attached to the zipper for a fixed time interval $t_{release}$, chosen to match the average time delay from when a junction joins the zipper to when the cell that contained that junction detaches from the zipper (see Figure S3C). When a cell detaches from the zipper, a new junction is formed with length L_{min} between its immediate neighbors and assigned the tension value of T_{behind} (Figure S3A). Finally, when junctions between epidermal cells become candidates for exchange, we allow a standard T1 exchange to occur in which the junction disappear and the cells containing that common junction become separated by a new

junction formed with length L_{min} between the common neighbors of those cells (Figure S3B). We chose a nominal value for L_{min} = 0.5 μm, but varying this value had little or no effect on the outcome of the simulations (not shown).

Choosing a value for the effective viscosity.

We assumed that the effective viscosity was the same for all cell-cell junctions and we fixed its value as follows. Given values for junction tensions, the frequency of primary contractions, and the probability of zipper release, we ran simulations and measured the average speed of primary junction shortening for different values of μ_{eff}, measuring contraction rate as the change in junction length from the initiation to completion of a primary contraction divided by the time to complete the contraction:

$$rate = \frac{L_{init} - L_{\min}}{\Delta t}$$

Then we chose a value for μ_{eff} that yielded a close match between the measured and simulated rates (Figure S3E).

Choosing reference values for other parameters.

For parameters governing the constant area constraints (β,β_{brain}) and the linkage of junction elements to tri-cell vertices (k_s) we used values that kept variation in cell surface area and gaps between junction elements at tri-cell vertices reasonably small (see Supplementary Experimental Procedures, Summary table below). Varying these values had no significant effect on the simulated dynamics, but increased the tendency towards numerical instability. Finally, by comparing simulation outcomes for decreasing values of

μ_g (relative to fixed μ_{eff}), we determined a value for μ_g that was large enough to allow efficient numerical solution of the equations of motion, but small enough that it did not significantly affect the simulated dynamics.

For the axial resistance coefficient k_{axial}, we chose a value sufficiently large to reduce axial shortening during a 4000 second simulation to less than 2.5% given reference values for junction tensions. We set the perpendicular resistance k_{perp} to 0, except during the sensitivity analysis shown in Figure S3I. We set the radial compression resistance β_{brain} to a value sufficiently large to reduce brain compression to less than 2.5% given reference values for junction tensions (Figure S3H).

Summary table of key parameter values.

Parameter	Symbol	Reference Value	Criteria for setting value
Primary Ne/Epi tension	T_1	0.19	From laser ablation (Figure 5) Normalized to primary tension value
Secondary Ne/Epi tension	T_2	0.12	From laser ablation (Figure 5) Normalized to primary tension value
Tertiary Ne/Epi tension	T_3	0.07	From laser ablation (Figure 5) Normalized to primary tension value

Tension on newly formed Epi/Epi junctions behind zipper	T_{behind}	0.1	From laser ablation (Figure 5) Normalized to primary tension value
Epi/Epi tensions	$T_{epi/epi}$	0.05	From laser ablation (Figure 5) Normalized to primary tension value
Axial resistance coefficient	k_{axial}	0.0002/μm^2	Set to minimum value sufficient to reduce axial shortening to < 2.5%
Perpendicular resistance coefficient	k_{perp}	0 /μm^2	Undetermined
Radial compression resistance coefficient (brain)	β_{brain}	0.003 /μm^3	Large enough to prevent compression of the brain by more than 2.5%
Time between primary contractions	$t_{contract}$	504 s	Measured *in vivo* Figure S3D
Time delay from junction merge to cell detachment	$t_{release}$	588 s	Measured *in vivo* Figure S3D
Effective viscosity	μ_{eff}	1.8 s	Determined by primary contraction speeds *in silico* and *in vivo*
Boundary friction	μ_g	0.003 s/μm^2	Determined asymptotically

Pressure force multiplier	β	0.3	Large enough to maintain $(A\text{-}A_0)/A_0 < 0.05$
Vertex spring constant	k_s	0.8	Sufficient to maintain gaps between vertex and boundaries < 0.2μm
Threshold length for merging junctions with zipper or initiating T1 exchange	L_{min}	0.25 μm	Nominal
Integration timestep	t_{step}	0.07	Set to maximum value that avoids numerical instability.

Supplementary References

Bausch, A. R., Möller, W. and Sackmann, E. (1999). Measurement of local viscoelasticity and forces in living cells by magnetic tweezers. *Biophys. J.* **76**, 573–579.

Bertrand, V., Hudson, C., Caillol, D., Popovici, C. and Lemaire, P. (2003). Neural tissue in ascidian embryos is induced by FGF9/16/20, acting via a combination of maternal GATA and Ets transcription factors. *Cell* **115**, 615–627.

Bray, D. and White, J. G. (1988). Cortical flow in animal cells. *Science* **239**, 883–888.

Corbo, J. C., Erives, A., Di Gregorio, A., Chang, A. and Levine, M. (1997). Dorsoventral patterning of the vertebrate neural tube is conserved in a protochordate. *Development* **124**, 2335–2344.

Farhadifar, R., Röper, J.-C., Aigouy, B., Eaton, S. and Jülicher, F. (2007). The influence of cell mechanics, cell-cell interactions, and proliferation on epithelial packing. *Curr. Biol.* **17**, 2095–2104.

Hotta, K., Mitsuhara, K., Takahashi, H., Inaba, K., Oka, K., Gojobori, T. and Ikeo, K. (2007). A web-based interactive developmental table for the ascidian Ciona intestinalis, including 3D real-image embryo reconstructions: I. From fertilized egg to hatching larva. *Dev. Dyn.* **236**, 1790–1805.

Mayer, M., Depken, M., Bois, J. S., Jülicher, F. and Grill, S. W. (2010). Anisotropies in cortical tension reveal the physical basis of polarizing cortical flows. *Nature* **467**, 617–621.

Munro, E. M. and Odell, G. (2002). Morphogenetic pattern formation during ascidian notochord formation is regulative and highly robust. *Development* **129**, 1–12.

Pasini, A., Manenti, R., Rothbächer, U. and Lemaire, P. (2012). Antagonizing retinoic acid and FGF/MAPK pathways control posterior body patterning in the invertebrate chordate Ciona intestinalis. *PLoS ONE* **7**, e46193.

Philips, A., Blein, M., Robert, A., Chambon, J.-P., Baghdiguian, S., Weill, M. and Fort, P. (2003). Ascidians as a vertebrate-like model organism for physiological studies of Rho GTPase signaling. *Biol. Cell* **95**, 295–302.

Robin, F. B., Dauga, D., Tassy, O., Sobral, D., Daian, F. and Lemaire, P. (2011). Time-lapse imaging of live Phallusia embryos for creating 3D digital replicas. *Cold Spring Harb Protoc* **2011**, 1244–1246.

Roure, A., Rothbächer, U., Robin, F., Kalmar, E., Ferone, G., Lamy, C., Missero, C., Mueller, F. and Lemaire, P. (2007). A multicassette Gateway vector set for high

throughput and comparative analyses in ciona and vertebrate embryos. *PLoS ONE* **2**, e916.

Sherrard, K., Robin, F., Lemaire, P. and Munro, E. (2010). Sequential activation of apical and basolateral contractility drives ascidian endoderm invagination. *Curr. Biol.* **20**, 1499–1510.